

Critical Metallicity of Cool Supergiant Formation. I. Effects on Stellar Mass Loss and Feedback

PO-SHENG OU (歐柏昇)^{1,2}, KE-JUNG CHEN (陳科榮)¹, YOU-HUA CHU (朱有花)^{1,2,3} AND SUNG-HAN TSAI (蔡松翰)^{1,2}

¹*Institute of Astronomy and Astrophysics, Academia Sinica, No.1, Sec. 4, Roosevelt Rd., Taipei 10617, Taiwan, R.O.C.*

²*Department of Physics, National Taiwan University, No.1, Sec. 4, Roosevelt Rd., Taipei 10617, Taiwan, R.O.C.*

³*Department of Astronomy, University of Illinois, 1002 West Green Street, Urbana, IL 61801, U.S.A.*

ABSTRACT

This paper systematically studies the relation between metallicity and mass loss of massive stars. We perform one-dimensional stellar evolution simulations and build a grid of ~ 2000 models with initial masses ranging between 11 and 60 M_{\odot} and absolute metallicities Z between 0.00001 and 0.02. Steady-state winds, comprising hot main-sequence winds and cool supergiant winds, are the main drivers of the mass loss of massive stars in our models. We calculate the total mass loss over the stellar lifetime for each model. Our results reveal the existence of a critical metallicity Z_c at $Z \sim 10^{-3}$, where the mass loss exhibits a dramatic jump. If $Z > Z_c$, massive stars tend to evolve into cool supergiants, and a robust cool wind is operational. In contrast, if $Z < Z_c$, massive stars usually remain as blue supergiants, wherein the cool wind is not activated and the mass loss is generally weak. Moreover, we calculate the wind feedback in a $10^5 M_{\odot}$ star cluster with the Salpeter initial mass function. The kinetic energy released by winds does not exhibit any significant transition at Z_c because the wind velocity of a cool supergiant wind is low and contributes little to the kinetic energy. The effects of critical metallicity provide implications for the fates of metal-poor stars in the early universe.

Keywords: Stellar mass loss — Massive stars — Cool supergiant stars — Metallicity

1. INTRODUCTION

Massive stars lose a substantial amount of mass via stellar winds, which inject energies and enriched material into the interstellar medium (ISM). Main-sequence OB stars can produce *hot winds* that are driven by the radiation pressure of the line emission (Puls et al. 2008; Vink 2021, for review), and red supergiants (RSGs) produce even stronger *cool winds* that are driven by the dust continuum (Willson 2000; Decin 2021, for review). The mass loss from these winds influences the evolutionary tracks and the fates of massive stars (Langer 2012; Smith 2014; Vink et al. 2015) and reshapes the ambient environment (e.g., Chu 2008).

The mass from the stripped-off envelopes of massive stars form circumstellar media (CSM). When a massive star explodes as a supernova (SN), it may interact with the CSM produced by its progenitor star. This interaction plays an important role in the SN observables (e.g., Smith 2014; Maeda et al. 2015; Moriya et al. 2017; Chen et al. 2020). If the SN explosion was preceded by a blue supergiant (BSG)

or Wolf-Rayet (WR) phase, its fast wind would have swept up the CSM to form a wind-blown bubble. The SN ejecta and shock wave will encounter the circumstellar bubble, and strongly affect the dynamical evolution of SNR (e.g., Dwarkadas 2005; Patnaude et al. 2017; Ou et al. 2018). Therefore, stellar winds have a profound impact on SNe and their resulting SNRs, which drive the ISM ecosystem.

On a larger scale, stellar winds serve as a critical ingredient of stellar feedback in galaxies (Abbott 1982; Leitherer et al. 1992; Freyer et al. 2003). Although the contribution of stellar winds is thought to be less powerful than that of SNe (e.g., Walch, & Naab 2015; Dale 2015), some ISM simulations indicate that stellar winds are more efficient than SNe in disrupting giant molecular clouds (Rogers, & Pittard 2013; Fierlinger et al. 2016; Rey-Raposo et al. 2017) and retaining energies in superbubbles (Krause et al. 2013). For cosmological simulations, stellar feedback is essential for reproducing the observed star-formation rates in galaxies, and appropriate expressions of stellar mass loss are often required (e.g., Stinson et al. 2006; Hopkins et al. 2014; Agertz, & Kravtsov 2015; Schaye et al. 2015; Wang et al. 2015; Hopkins et al. 2018; Pillepich et al. 2018; Springel et al. 2018; Emerick et al. 2019; Marinacci et al. 2019; Hopkins et al. 2022).

To evaluate the energy feedback of massive stars, we need to consider the total mass loss and total kinetic energy injected by stellar winds. The mass loss rate (\dot{M}) of a stellar wind depends on metallicity (Z), and the dependence is typically expressed as $\dot{M} \sim Z^m$, where m is a constant (e.g., Vink et al. 2001; Mokiem et al. 2007; Mauron & Josselin 2011). In the aforementioned cosmological simulations, a single-value Z appropriate for a particular epoch is used for the \dot{M} and energy feedback estimates. It is well known that Z can strongly impact the evolutionary tracks of stars (El Eid et al. 2009; Maeder 2009; Langer 2012), and Z varies along the stellar evolution tracks. It is conceivable that the dependence of \dot{M} on Z varies along the stellar evolution tracks. To estimate the total mass loss (ΔM) of a massive star, it is necessary to integrate the \dot{M} for its contemporary Z over the entire evolutionary track. Likewise, the total kinetic energy injected by a massive star’s stellar winds has to be determined by integrating the wind mechanical luminosity over the evolutionary track using \dot{M} and wind velocity appropriate for their contemporary Z .

Previous calculations of ΔM of massive stars have been carried out for a wide range of initial masses (e.g., Limongi 2017; Renzo et al. 2017; Beasor & Davies 2018). It is found that different wind prescriptions cause $\sim 50\%$ uncertainties in the resulting ΔM (Renzo et al. 2017). Recently, Fichtner et al. (2022) calculated the total mass and energy released by stellar winds within a star cluster and showed that they generally increase with metallicity; they also found that the rate of increase is quite different for single and binary stars. The above studies either considered an entire cluster or included only a small number of discrete Z values; thus they do not allow a detailed examination of metallicity effects.

We have systematically studied the metallicity effects on the total mass loss and kinetic energy release of massive stars by employing the MESA code to perform a series of stellar evolution simulations. We establish models of single non-rotating stars with wind physics. The numerical methods and stellar wind prescriptions are described in Section 2. Based on this model grid, we describe the general features of stellar evolution in Section 3. Then in Section 4, we present the main results of the total mass loss as a function of the initial mass and metallicity of massive stars. We report a *critical metallicity* (Z_c) of mass loss and show that it is associated with the cool supergiant formation. In Section 5 we calculate the energy feedback of winds using our grid of models. Finally, we discuss the implications of our results in Section 6 and present the conclusions in Section 7. In the companion Paper II, we will further investigate the physical mechanism of Z_c and explain it according to the fundamental understanding of cool supergiant formation.

2. METHODOLOGY

In this section, we introduce the stellar evolution code for building our models, describe the prescriptions of stellar mass loss, and summarize the parameter space of our models.

2.1. MESA Code

We perform massive-star evolution simulations using the Modules for Experiments in Stellar Astrophysics (MESA; Paxton et al. 2011, 2013, 2015, 2018, 2019) version No.10108. We primarily use `MESASstar`, a 1D stellar evolution code that can model stellar evolution from the pre-main-sequence stage to the zero-age main sequence (ZAMS) stage, and from the ZAMS to the iron core-collapse stage. It hydrodynamically evolves stars using microphysics such as nuclear reaction networks, equations of state, and opacities, which are the key physics of stellar evolution and are available in MESA.

MESA provides several stellar wind functions that can be used to calculate the mass-loss rates using stellar parameters at each timestep during the stellar evolution. When a mass-loss routine is turned on, the code adjusts the stellar structure by rescaling the mass coordinates of the mass cells, according to the mass-loss rate given by the wind functions (Paxton et al. 2011).

2.2. Physical Processes

Our simulations include two steps. First we evolve a pre-main-sequence star to reach the ZAMS stage, and then, we use the ZAMS model as the initial condition in the stellar evolution and evolve the model from the main sequence to the end of the star’s life. Different nuclear reaction networks are employed in these two steps. For the pre-main-sequence evolution, we simply adopt the “basic” network with eight isotopes. For the evolution from the ZAMS stage onward, we employ the more complicated nuclear reaction network “approx21 (Cr60),” which includes 21 isotopes¹.

In the stellar evolution simulations, we mainly use the default parameters for massive stars in the “in-list_massive_defaults” file in the `MESASstar` module. Additionally, the Ledoux criterion and Henyey’s mixing-length theory (Henyey et al. 1965) are applied, and the mixing-length scaling parameter α (i.e., the ratio of mixing length to pressure scale height) is set at 1.5. The Type 2 OPAL opacity tables (Iglesias & Rogers 1996) are applied during and after the helium burning. In addition to the default parameters, we limit the change of helium abundance per timestep to $\leq 10\%$ to prevent abrupt changes.

2.3. Mass-Loss Prescriptions

¹ ¹H, ³He, ⁴He, ¹²C, ¹⁴N, ¹⁶O, ²⁰Ne, ²⁴Mg, ²⁸Si, ³²S, ³⁶Ar, ⁴⁰Ca, ⁴⁴Ti, ⁴⁸Cr, ⁵²Fe, ⁵⁴Fe, ⁵⁶Fe, ⁵⁶Ni, ⁶⁰Cr, proton, neutron

Although the mass-loss rates can be calculated using theoretical approaches (e.g., Vink et al. 2000, 2001), such calculations are time-consuming and only available for hot winds. Instead, simple formulae of the mass-loss rates derived from observations or theoretical calculations are usually adopted in stellar evolution. Most of these widely used mass-loss prescriptions have been built in as modules in MESA. In our stellar evolution simulations, we apply the hot wind prescription of Vink et al. (2000, 2001, hereinafter, V01), cool wind prescription of de Jager et al. (1988, hereinafter, dJ88), and WR wind prescription of Nugis & Lamers (2000, hereinafter, NL00). These prescriptions are described below.

For hot OB stars, metal ions in the stellar atmospheres absorb photons in the ultraviolet (UV) resonance lines and are radiatively accelerated, yielding steady-state winds (Lucy & Solomon 1970; Castor et al. 1975; Puls et al. 2008). Using multi-line radiative transfers calculated by the Monte Carlo methods (Abbott & Lucy 1985), Vink et al. (2000, 2001) presented a grid of wind models, fitted the models with a linear regression, and established a mass-loss prescription for hot stars with effective temperatures $T_{\text{eff}} > 10^4$ K.

When a massive star evolves into an RSG, its cool wind is driven by the radiation pressure on dust grains, similar to the winds from the asymptotic-giant-branch stars. To date, although empirical laws have been established, no well-established theoretical predictions for cool winds exist, because the origin and structure of RSG winds are very complex and the cool wind mechanism is poorly understood (Smith 2014). Among the mass-loss rates suggested by the various empirical laws, up to a factor of 10 scatter has been seen (dJ88; Reimers 1975; Nieuwenhuijzen & de Jager 1990; van Loon et al. 2005; Maun & Josselin 2011; Goldman et al. 2017; Beasor & Davies 2018; Beasor et al. 2020; Humphreys et al. 2020). In our simulations, we adopt the most commonly used cool-wind prescription by dJ88, which is an empirical function based on the fitting of the observed mass-loss rates of a set of O–M stars. Although $\dot{M} \sim Z^m$ has been included in some recent cool wind functions (e.g., Maun & Josselin 2011; Groh et al. 2019), the exponent m is uncertain. Recent observations have shown that the mass-loss rates of RSGs are nearly independent of metallicity (Goldman et al. 2017; Beasor et al. 2020). Therefore, we adopt the dJ88 prescription without metallicity dependence available in MESA, similar to other works such as Choi et al. (2016).

WR stars have $T_{\text{eff}} > 10^4$ K, but their mass-loss rates are a factor of 10 higher than those of hot O stars exhibiting the same luminosity (Nugis & Lamers 2002); thus, the hot-wind prescription is not suitable for them. We adopt the WR wind prescription by NL00, which is an empirical law of mass-loss rate as a function of luminosity, helium abundance, and metallicity. It was derived from the observations of 64 Galactic WR stars with the correction of clumping in the wind.

This prescription is supported by an optically thick radiation-driven wind theory (Nugis & Lamers 2002).

The hot, cool, and WR wind schemes operate under different stellar evolution stages. The switches between different wind schemes depend on T_{eff} and the surface hydrogen abundance (X_H) of the simulated stars. The wind prescriptions are explained in detail in Appendix A.

In the “Dutch” hot/WR wind scheme in MESA, a “low-T” regime is present where the dJ88 prescription is adopted rather than the V01 prescription. For simplicity, we use the term “hot wind” to denote only the mass loss derived from the V01 prescription, and use the term “cool wind” to denote all the mass loss derived from the dJ88 prescription.

2.4. Stellar Evolution Simulations

We establish a set of models to investigate the influence the initial mass and metallicity on the stellar mass loss. In our grid, the initial mass values are sampled successively in the range of 11–60 M_{\odot} with 1- M_{\odot} steps. Moreover, 38 different values of initial absolute metallicities Z are chosen: $Z = (1, 2, \dots, 9) \times 10^{-5}$, $(1, 2, \dots, 9) \times 10^{-4}$, $(1, 2, \dots, 9) \times 10^{-3}$, and $(1.0, 1.1, 1.2, \dots, 2.0) \times 10^{-2}$. For reference, the solar metallicity is $Z_{\odot} = 1.34 \times 10^{-2}$ (Asplund et al. 2009). Overall, the total number of models in our grid is 1900.

Our stellar models are typically evolved until the iron core-collapse stage. However, some models with initial masses of 11–17 M_{\odot} stall at the carbon or oxygen burning stages, usually because of abrupt changes in abundance that cannot be easily treated numerically. As these stars have already passed the RSG phase, we adopt the masses at this point as the final masses.

We perform our simulations using the TIARA-TC cluster² maintained by the Institute of Astronomy and Astrophysics, Academia Sinica (ASIAA). This cluster has 50 nodes, 600 CPU cores, and 2.3 TB memory. Our grid simulations were completed in about 100,000 core-hours.

3. STELLAR EVOLUTION AND MASS LOSS RATE

Stellar mass loss depends on the physical parameters of stars, which vary along the stellar evolution. In this section, we first describe the stellar evolution and then their associated mass loss.

3.1. Stellar Evolution

We perform simulations of stellar evolution with different initial masses and metallicities. Their evolutionary tracks in the theoretical Hertzsprung–Russell (HR) diagram, i.e., luminosity (L) versus T_{eff} diagram, are shown in the left panels of Figure 1. During the main-sequence phase of 20–60 M_{\odot}

² <https://www.tiara.sinica.edu.tw/facility.php>

stars, T_{eff} decreases by 0.1–0.25 dex and L increases by 0.3–0.15 dex over the main-sequence lifetime of $\sim 8\text{--}4$ Myr. A star reaches the terminal-age main sequence (TAMS) when the hydrogen in its stellar core is exhausted. At this time, a hydrogen-burning shell forms, the star starts expanding, and T_{eff} quickly decreases. Then, the core-helium burning starts, and the outer envelope continues to expand and becomes much cooler. In the HR diagram, the star quickly crosses the “Hertzsprung gap” and moves to the right side. After these post-main-sequence evolution stages, the star becomes a supergiant. Supergiants with $\log(T_{\text{eff}}/\text{K}) < 3.6$ (or $T_{\text{eff}} \lesssim 4,000$ K) are often called RSGs, $3.6 < \log(T_{\text{eff}}/\text{K}) < 3.8$ (or $4,000 \text{ K} \lesssim T_{\text{eff}} \lesssim 6,300 \text{ K}$) are called yellow supergiant (YSGs), and $\log(T_{\text{eff}}/\text{K}) > 3.8$ (or $T_{\text{eff}} \gtrsim 6,300 \text{ K}$) are called BSGs (e.g., Georgy 2012).

A star’s lowest T_{eff} in its evolutionary track depends on its initial mass and metallicity. As shown in Figure 1, for stars with $Z = 0.02$, those with initial masses $\gtrsim 50 M_{\odot}$ can only become YSGs instead of RSGs. Furthermore, comparison of the models of $Z = 0.02$ and $Z = 0.0005$ shows that the evolutionary tracks of lower- Z stars usually end at higher T_{eff} . This feature is critical in the relation between mass loss and metallicity, and will be elaborated in later sections. For convenience, we use the term “cool supergiant” as long as the dJ88 wind prescription is fully active, i.e. $T_{\text{eff}} < 10,000 \text{ K}$, or $\log(T_{\text{eff}}/\text{K}) < 4.0$.

During the advanced burning stages, stars with initial masses $\gtrsim 50 M_{\odot}$ can reach luminosities $\gtrsim 10^6 L_{\odot}$. These stars can be regarded as luminous blue variables (LBVs) (Humphreys, & Davidson 1994), but our simulations do not include eruptive mass loss, which is a common feature of LBVs. Furthermore, some LBVs lose their envelopes and evolve back to a hotter region in the HR diagram to become WR stars. We use the criterion of surface hydrogen abundance (X_S) below 0.4 to identify WR stars in our work.

3.2. Evolution of Mass Loss Rate

As a star evolves through different burning phases, its T_{eff} and radius vary, resulting in different types of stellar winds and mass-loss rates. As described in Section 2.3, the mass-loss rates are calculated using a combination of mass-loss prescriptions chosen according to T_{eff} and X_S . In the HR diagrams in Figure 1, most high- Z and some low- Z stars shift from the hot wind region to the cool wind region in the post-main-sequence stage. The massive stars of 50 and 60 M_{\odot} with $Z = 0.02$ further evolve back to the hot region and enter the WR phase. The criterion $X_S < 0.4$ is used to activate the WR wind scheme.

The right panels of Figure 1 present the evolution of the mass-loss rates in our stellar evolution simulations. During the main-sequence phase, $\log T_{\text{eff}}$ is in the range of $\sim 4.45\text{--}4.75$, and thus, hot winds dominate. For models of

the same Z , higher-mass stars have higher luminosities and higher mass-loss rates; furthermore, a main-sequence star’s mass-loss rate is usually low and stable because the T_{eff} and luminosity changes are not large. For models of different Z but the same initial mass, a higher Z leads to a higher mass-loss rate, but the \dot{M} dependence on Z is not a simple Z^m because \dot{M} also depends on L and T_{eff} , which are also dependent on Z . For $Z = 0.0005$, \dot{M} for 20–60 M_{\odot} main-sequence stars is in the range $\sim 10^{-8}\text{--}10^{-6} M_{\odot} \text{ yr}^{-1}$, and for $Z = 0.02$, $\sim 10^{-7.5}\text{--}10^{-5.5} M_{\odot} \text{ yr}^{-1}$. When a star evolves into the post-main-sequence stage, T_{eff} suddenly decreases. The change in T_{eff} causes the enhancement of mass-loss rate by about 1–3 orders of magnitude, because the T_{eff} passes through two jumps in the mass-loss rate included in the wind prescriptions. These two jumps correspond to two physical transitions in the supergiant winds:

(1) *The “bi-stability jump” in early-type supergiant winds.* When the T_{eff} is less than $\sim 25,000 \text{ K}$, the mass-loss rate suddenly increases and the wind velocity decreases, which is called the “bi-stability jump” (Pauldrach & Puls 1990). This is caused by the recombination of Fe IV. When the temperature decreases below $\sim 25,000 \text{ K}$, the ionization fraction of Fe III below the sonic point significantly increases, and Fe III lines are more efficient drivers of winds than Fe IV lines (Vink et al. 1999). The mass-loss prescription of V01 illustrates the bi-stability jump by setting different mass-loss functions in the two regimes with T_{eff} values higher and lower than the jump temperature, which ranges between 22,500 and 27,500 K.

(2) *The transition from hot winds to cool supergiant winds.* When the T_{eff} decreases below 10,000–12,000 K, the star evolves into a cool supergiant. The cool, dust-driven wind becomes the dominating means of mass loss, and the mass-loss rate significantly increases.

These two jumps in the mass-loss rate occur at the post-main-sequence stage, marked as the bi-stability jump and the hot-to-cool wind transition region in Figure 1. The stellar evolution timescale between these two jumps are usually so short, $< 10^4 \text{ yr}$, that these two jumps are unresolvable in the evolution of mass loss rate plots (the right panels of Figure 1).

Nevertheless, for some low- Z stars with $Z = 0.0005$, their T_{eff} only decreases to the range between 10,000 and 25,000 K at the onset of the post-main-sequence stage, and they remain as early-type supergiants. Some of the other low- Z stars do cool down to $T_{\text{eff}} < 10,000 \text{ K}$, but this happens in the very late evolutionary stage after the core-carbon burning commences; thus, the separation between the two jumps is about several hundred thousand years. For example, for the star with 30 M_{\odot} and $Z=0.0005$, the second jump in the mass-loss rate occurs at the very end of its lifetime.

4. TOTAL MASS LOSS AND METALLICITY

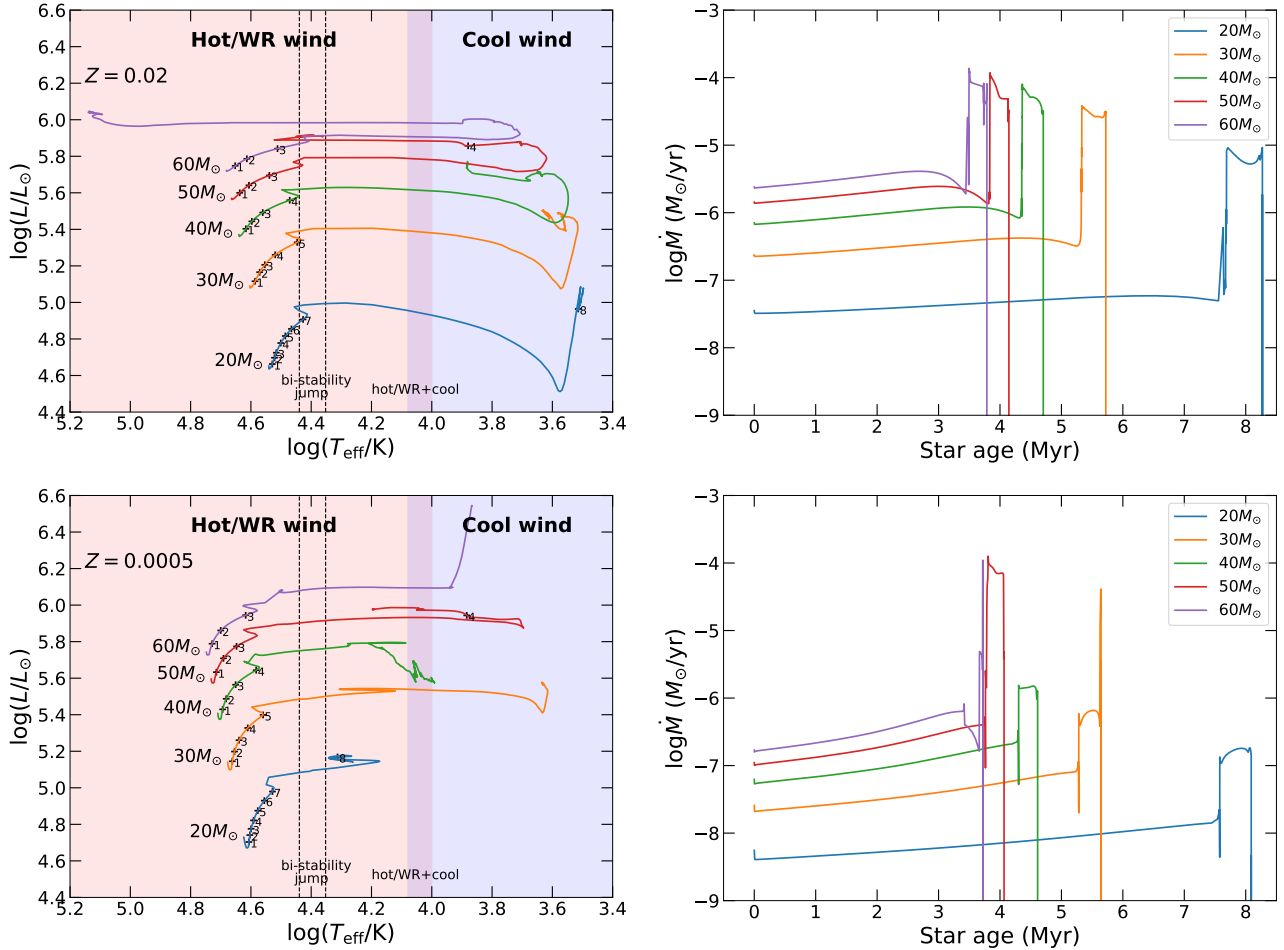


Figure 1. The HR diagram of massive stars and their mass-loss histories. *Left panels:* the stellar evolutionary tracks of 20–60 M_{\odot} stars with $Z = 0.02$ and 0.0005 . The region between dashed lines denotes the temperature range of the bi-stability jump. The red and blue regions represent hot and cool winds, respectively, instead of the colors of stars. When $10,000 \text{ K} < T_{\text{eff}} < 12,000 \text{ K}$, a combination of hot and cool winds is adopted. The “+” marks and the numbers beside them record the stellar ages in the unit of Myr. *Right panels:* The evolution of the mass-loss rates of stars with absolute metallicities $Z = 2 \times 10^{-2}$ (*top panel*) and $Z = 5 \times 10^{-4}$ (*bottom panel*). The mass loss of massive stars depends on their initial masses and metallicities, and their mass-loss rates in the post-main sequence can be $10^3 - 10^4$ higher than those in the main sequence.

Since stellar mass loss is very sensitive to the evolutionary phases, the total mass loss in the lifetime of a star depends on its initial mass and metallicity. This section presents our results of the total mass loss integrated through stellar lifetimes.

4.1. Initial Mass and Metallicity Dependence of Mass Loss

Figure 2 displays representative relations between a star’s initial mass (M_i) and the total mass loss (ΔM), which is the integrated mass loss over the stellar lifetime. The total mass loss generally increases with the initial stellar mass, but the detailed relation depends on the metallicity. At a first glance, three different trends of mass loss are observed at different metallicities:

(1) For $Z \gtrsim 5 \times 10^{-3}$, the high- Z cases, the total mass loss of a star generally increases with its initial mass. For ex-

ample, for $Z = 0.02$ ($> 1Z_{\odot} = 0.0134$), a $15M_{\odot}$ star loses $\sim 2M_{\odot}$, and a $60M_{\odot}$ star loses $> 30M_{\odot}$ during its lifetime.

(2) For $Z \lesssim 3 \times 10^{-4}$, the low- Z cases, the total mass loss of a star also increases with its initial mass, but it is considerably lower than that of the $Z \gtrsim 10^{-2}$ cases. For example, for $Z = 10^{-4}$, a $15M_{\odot}$ star loses $\sim 0.01M_{\odot}$, and a $60M_{\odot}$ star loses $\sim 0.5M_{\odot}$. Some low- Z high-mass stars have high mass losses, but their total mass loss is still $< 20\%$ of the initial mass.

(3) For stars with $Z \sim 10^{-3}$, the total mass loss is not a smooth function of the initial mass; instead, it oscillates between the high values for the high- Z cases and the low values for the low- Z cases.

4.2. Critical Metallicity

We have shown that the total mass loss during a star’s lifetime largely depends on its metallicity. To further illustrate

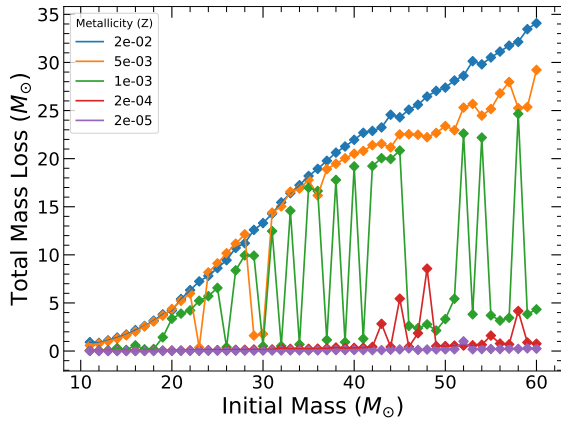


Figure 2. Total mass loss as a function of the initial mass for stars with different initial metallicities.

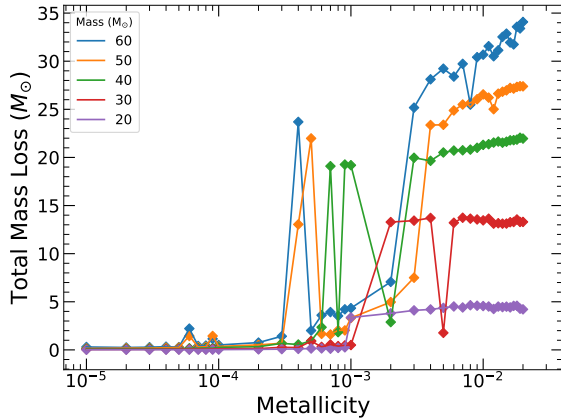


Figure 3. Total mass loss as a function of initial metallicity for stars with different initial masses.

the metallicity effects on mass loss, we plot the total mass loss as a function of metallicity in Figure 3.

Figure 3 displays a significant jump in the total mass loss at $Z \sim 10^{-3}$. When $Z \lesssim 3 \times 10^{-4}$, the mass loss is generally low. When Z approaches $\sim 10^{-3}$, the mass loss jumps to a significantly higher level.

Herein, we call the $Z \sim 10^{-3}$ as the critical metallicity (Z_c) for the mass loss of massive stars. Generally, significant mass loss occurs only when $Z > Z_c$. Nonetheless, Z_c is not a sharp boundary as shown in the stellar initial mass versus metallicity ($M_i - Z$) diagram of mass loss fraction ($\Delta M/M_i$) in Figure 4, where all the 1900 models are included. Two distinct regions are present in this diagram: the high- Z region with mass loss fraction $\gtrsim 40\%$ and the low- Z region with mass loss fraction $\lesssim 10\%$. The separation of the high- Z and low- Z regions is clear, and the boundary at $Z \sim 10^{-3}$ is what we

call Z_c . For initial masses $\lesssim 30M_\odot$, the boundary between these two regions is sharp; for initial masses $\gtrsim 30M_\odot$, the boundary is fuzzy.

4.3. Mass Loss from Different Wind Schemes

To understand the origin of Z_c , we compare the individual contributions of mass loss by hot, cool, and WR winds in order to identify a specific stellar evolutionary stage that is most accountable for Z_c . Figure 5 displays the contributions of different winds for initial stellar masses of 25 and 50 M_\odot . In both cases, a distinct jump in the mass loss occurs only in the cool wind near Z_c , indicating that the cool wind is responsible for Z_c .

The $M_i - Z$ diagrams of mass loss fraction for hot, cool, and WR winds are presented in Figure 6. For cool winds, going from high Z to low Z , the high mass loss makes a sharp transition into a low mass loss near a threshold Z of $\sim 1 \times 10^{-3}$. The threshold Z is slightly lower for stars with $M_i = 25 - 30M_\odot$ and higher for the more massive stars. For hot winds, the transition of high mass loss to low mass also occurs near a threshold Z of 1×10^{-3} , but the transition is gradual. For WR winds, the threshold Z is higher, near 3×10^{-3} . As the total contribution of hot and WR winds to the mass loss is small, $\Delta M/M_i \lesssim 20\%$, the $M_i - Z$ diagram of cool wind is very similar to that of the total mass loss (all winds combined) in Figure 4; furthermore, the Z_c of the total mass loss is similar to the threshold Z of the cool winds. It should be noted that at low Z , the hot winds may lose more mass than the cool winds up to the threshold Z of the cool winds; however, the mass lost via hot winds is so much smaller than the mass lost via cool winds that the cool winds' threshold Z dominates.

Therefore, Z_c of mass loss mainly stems from cool winds. This result is reasonable because the mass-loss rates of cool winds are usually considerably higher than those of hot winds, as included in the wind prescriptions (Section 3.2).

4.4. Cool Supergiants and the Critical Metallicity

We have shown that the mass-loss fraction ($\Delta M/M_i$) of a massive star is high for high Z and low for low Z , making a transition at Z_c that is caused mainly by the cool winds. To gain more insights into the dichotomy of mass-loss fraction and its scatter around Z_c , we use 25 M_\odot and 50 M_\odot stars with different metallicities that are near Z_c as examples, and look into their post-main-sequence evolution. For each stellar mass, five models with $Z = 0.0005, 0.0008, 0.001, 0.002,$ and 0.005 are examined. These models are marked by white dots in Figure 4. It can be seen that the 25 M_\odot stars show monotonic increase of mass loss fractions with increasing Z , while the 50 M_\odot stars show non-monotonic variations of mass loss fraction across Z_c . We deliberately choose these two masses with contrasting mass loss variations across Z_c ,

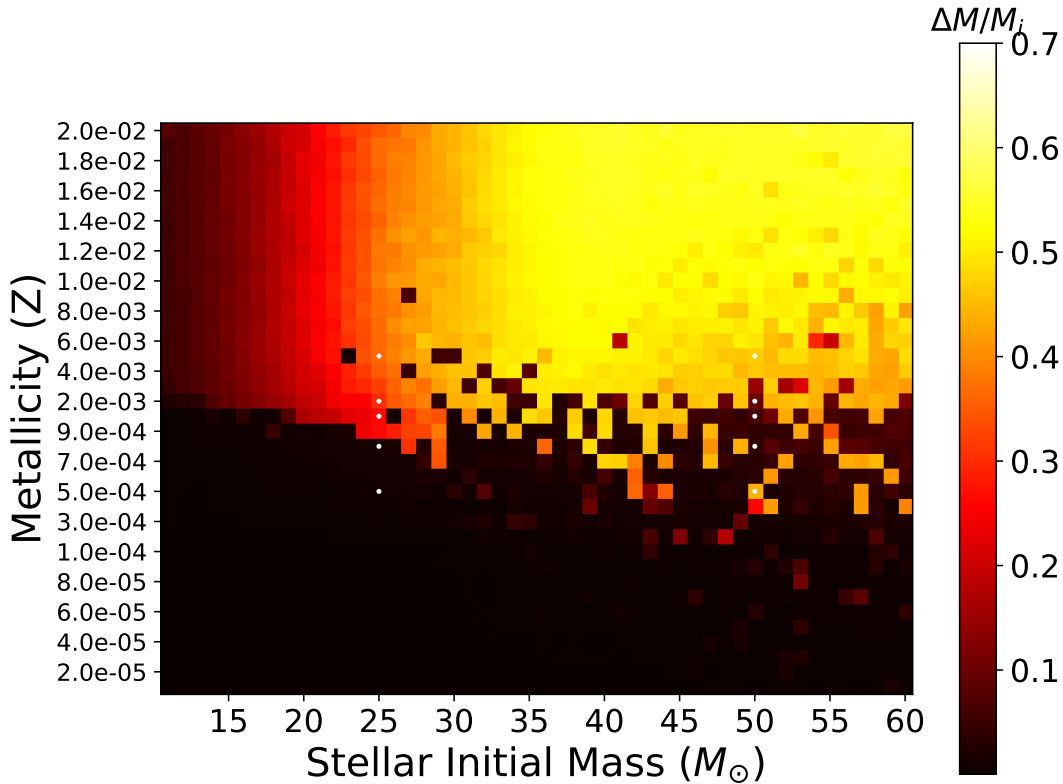


Figure 4. Fraction of total mass loss in each of our 1900 models is shown in the initial mass–metallicity phase diagram. The color scale represents the fraction of initial mass that is lost before a star dies. Each pixel in this map represents a stellar model. Note that the scale of the y-axis is nonuniform. A significant transition of the fraction value exists around $Z \sim 10^{-3}$, which separates the bright (high- Z) and dark (low- Z) sides of the map. This transition is called the *critical metallicity*. The white dots mark the models chosen in Section 4.4 to investigate the origin of the critical metallicity.

and expect the comparison between them may shed light on the physical origin of the transition and the scatter of mass loss fraction near Z_c .

To investigate the crucial differences among these models, we plot their stellar evolutionary tracks and mass-loss rates in Figure 7. For the $25 M_\odot$ stars, the three models yielding high ΔM ($Z = 0.001, 0.002,$ and 0.005) are those that evolve to radii $R > 1,000 R_\odot$ and $\log(T_{\text{eff}}/\text{K}) < 3.6$ (i.e., $T_{\text{eff}} < 4,000$ K). In other words, these stars end their lives as RSGs. Due to stellar expansion, their mass-loss rates increase by 2–3 orders of magnitude in the supergiant stages. In contrast, the two models yielding in low ΔM ($Z = 0.0005$ and 0.0008) only expand to $\sim 100 R_\odot$. After moderate expansions, they bounce back to the left (i.e., higher T_{eff}) in the HR diagram, and their T_{eff} remains higher than $\sim 10,000$ K. Such a high T_{eff} prevents the cool wind from operating, and thus, their mass-loss rates only slightly increase during the post-main-sequence stages. In summary, the two different behaviors of stellar expansion result in the dichotomy of the total mass loss.

For the $50 M_\odot$ stars, the evolutionary tracks are more complicated. At the age of 4 Myr (marked by “+” in the HR

diagram in Figure 7), the two models yielding high ΔM ($Z = 0.0005$ and 0.005) have already evolved into the cool-wind domain, and eventually expand to $R > 1,000 R_\odot$. On the other hand, the three models yielding low ΔM ($Z = 0.0008, 0.001,$ and 0.002) are still in the hot-wind domain at 4 Myr. These three models eventually enter the cool-wind domain at the very end of their lifetimes when the core-carbon burning commences, and approach a high mass-loss rate of $\sim 10^{-4} M_\odot \text{ yr}^{-1}$. However, their cool winds only last a few $\times 10^4$ yr. Thus, the integrated ΔM is still small, yielding $\Delta M/M_i < 10\%$.

The above examples demonstrate that the crucial process that determines the total mass loss is the expansion toward the formation of a supergiant. If a star expands to a cool supergiant with $R > 1,000 R_\odot$ at the beginning of the post-main-sequence stage, significant mass loss will occur. Otherwise, if a star never expands to the extent of a cool supergiant or only expands to that extent at a very late stage (i.e., after the core-carbon burning begins), only a minimal amount of mass loss will occur.

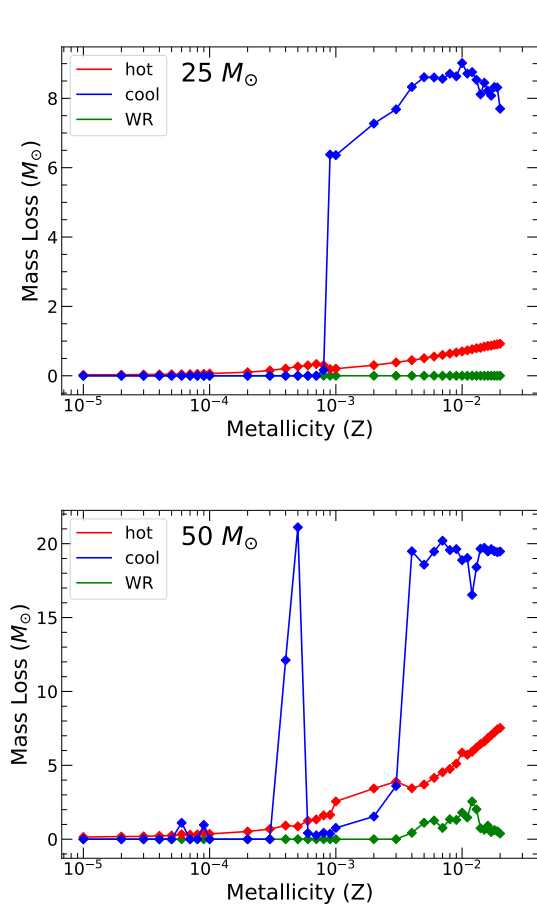


Figure 5. Contributions of the hot, cool, and WR winds to the total mass loss of 25 and $50 M_{\odot}$ stars. The significant jump in mass loss at $Z \sim 10^{-3}$ mainly arises from cool winds.

The crucial role played by the supergiant expansion in the dichotomy of mass loss is further illustrated in Figure 8, which presents maps of maximum radii in the $M_i - Z$ grid. We have considered maximum radii over two time spans: the entire lifetime (left panel of Figure 8) and the time span from the ZAMS to the beginning of core carbon burning (right panel of Figure 8). The left panel shows a complex map with a visible dichotomy only for stellar masses of $14-27 M_{\odot}$. The complexity stems from the maximum radii arising from different evolutionary stages and paths for stars of different masses. For high metallicities ($Z > Z_c$), stars reach maximum radii during the core helium burning; while for low metallicities ($Z < Z_c$), $14-27 M_{\odot}$ stars reach the maximum radii during the core helium burning, but the higher mass stars reach maximum radii after the core carbon burning. The core carbon burning stage is pretty late in a massive star’s lifetime, and the duration for high mass loss rate is short; thus, massive stars reach maximum radii during the core carbon burning stage have small mass loss fractions. The complications at the core carbon burning stage makes the maximum radius

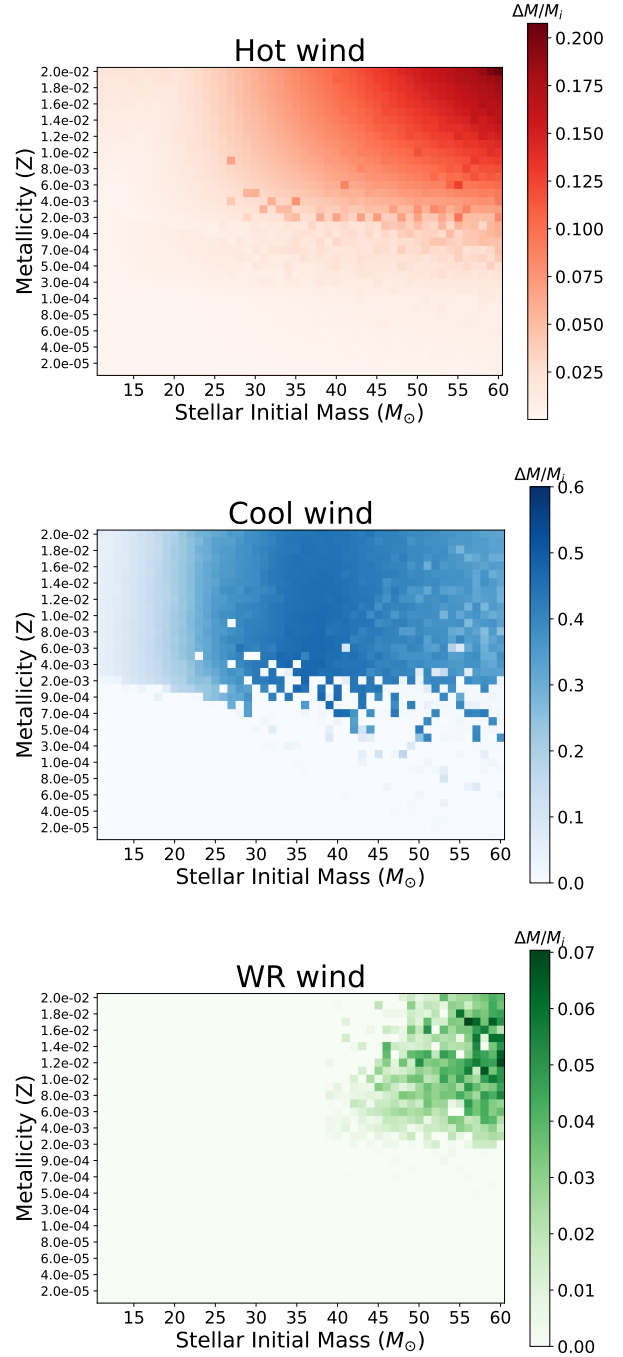


Figure 6. Fractions of mass loss to the initial masses caused by the hot, cool, and WR winds. These diagrams are similar to Figure 4, but the three wind components are separately plotted.

over the entire lifetimes an ineffective indicator of total mass loss.

As the core helium burning stage lasts the longest after the main sequence, and the bulk of mass loss occur during this stage, we next consider the maximum stellar radii during the time span from the ZAMS to the beginning of core carbon

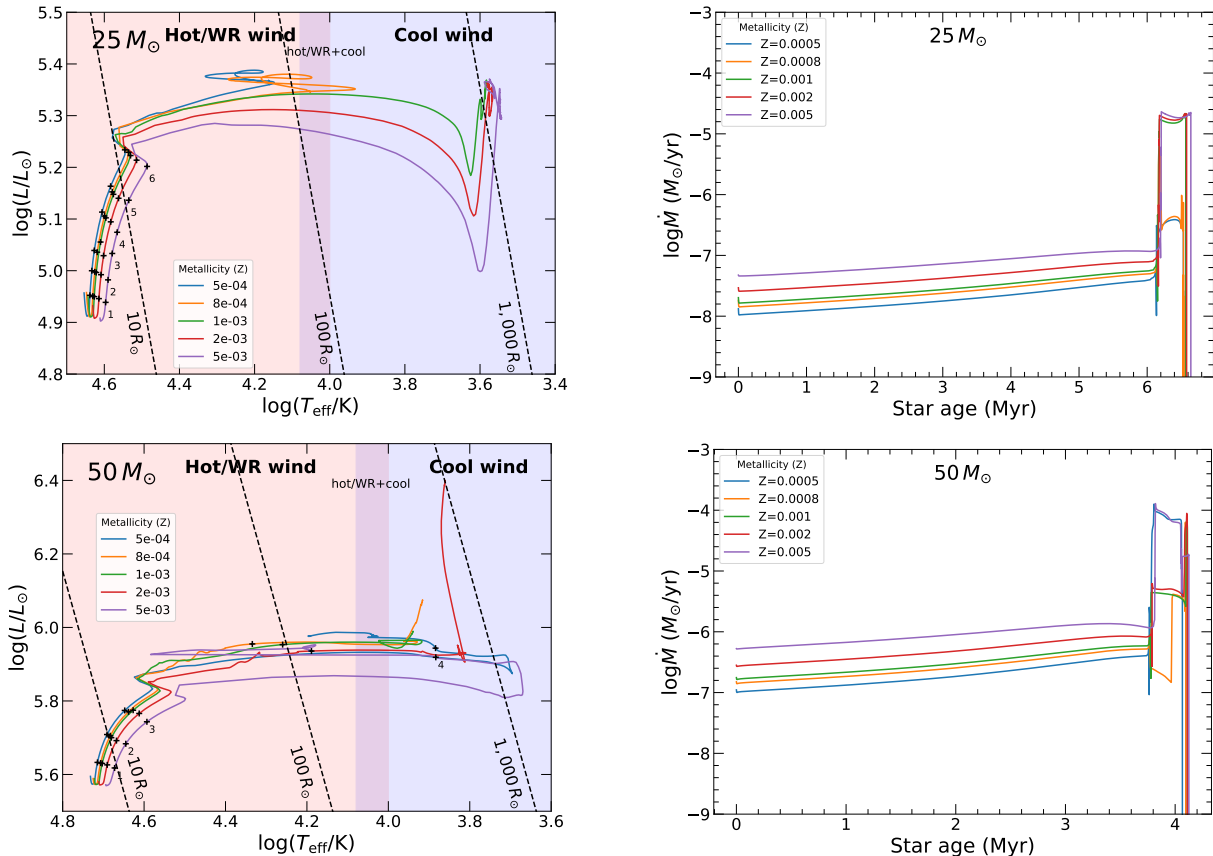


Figure 7. Evolutionary tracks (*left panel*) and mass-loss rates (*right panel*) of 25 and 50 M_{\odot} stars with different Z that are all near the critical metallicity. The bimodal behavior of the mass loss corresponds to two different trends of evolutionary tracks; the high-mass-loss models are those that successfully evolve into cool supergiants at the beginning of the post-main-sequence stage.

burning. In the right panel of Figure 8, a cleaner dichotomy is seen and the transition occurs near $Z_c \sim 0.001$. In fact, this map of maximum stellar radii resembles closely the map of mass loss fraction (Figure 4): both show dichotomy across the $Z_c \sim 0.001$ and larger scatter around Z_c at high stellar masses. Examined closely, even the scatter exhibits one-to-one correspondences between these two maps. These similarities indicate that the maximum stellar radius before core carbon burning is an effective indicator of total mass loss.

We further find that models with high mass loss are almost exactly those that have expanded to cool supergiants with $R > 1,000R_{\odot}$ at the core-helium burning stage, and these models are usually of $Z \gtrsim 10^{-3}$. Therefore, we conclude that the Z_c of mass loss is essentially the *critical metallicity of cool supergiant formation*.

Generally, cool supergiant formation and the corresponding mass loss only occur when Z is higher than the critical metallicity ($Z_c \sim 10^{-3}$). For stars with $Z > Z_c$, they usually expand to $R > 1,000R_{\odot}$ and become cool supergiants at the beginning of the post-main-sequence stage. These stars can lose large amounts of mass due to cool winds. In contrast, stars with $Z < Z_c$ either do not reach $R > 1,000R_{\odot}$ through-

out their lifetimes or only expand to this extent at the very final stage of stellar evolution. For these low- Z stars, the cool wind scheme is not activated in most of their stellar lifetime; thus, their total mass loss is very low. For $Z \sim Z_c$, a star either succeeds or fails to become a cool supergiant, and thus show erratic variations of the total mass loss as a function of metallicity (Figure 2 and 4). The physical mechanism that determines whether a star can become a cool supergiant will be investigated in our Paper II.

5. FEEDBACK FROM STELLAR WINDS

Our grid of stellar evolution models can be used to determine the feedback from stellar winds. We first compute the kinetic energy released by winds from individual stars, then consider the wind energy feedback for a star cluster. For star clusters we investigate the metallicity dependence of the total mass and kinetic energy injected by stellar winds into the ISM, and the evolution of mass and energy injection rates.

5.1. Kinetic Energy Released by Winds

The flux of kinetic energy carried by a stellar wind is called mechanical luminosity of the wind, defined as $L_w \equiv \frac{1}{2} \dot{M} v_{\infty}^2$, where v_{∞} is the wind terminal velocity. The determination

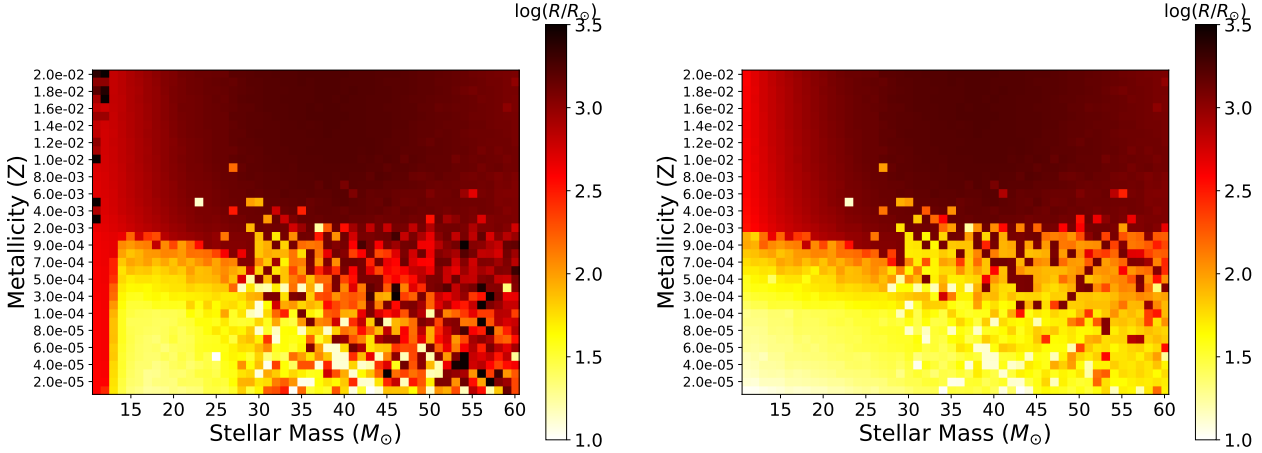


Figure 8. Maximum stellar radius of each model in the entire stellar lifetime (*left panel*) and before the core-carbon burning commences (*right panel*). The distribution of values in the right panel is almost identical to that in Figure 4, indicating that the low- Z models with negligible mass loss are those that fail to expand to cool supergiants before the core-carbon burning commences.

of \dot{M} has already been described in Section 2. Our stellar evolution models do not provide v_∞ directly, but provide escape velocity (v_{esc}) that can be scaled to determine v_∞ . For hot winds, we follow V01 and directly use the v_∞/v_{esc} scaling relations given in Eq. A1 and A2 in Appendix A. For cool winds, we follow Leitherer et al. (1992) and set the RSG wind terminal velocity at a constant 30 km s^{-1} . More details of v_∞/v_{esc} can be found in Appendix A. A star's \dot{M} and v_∞ are used to compute L_w , then L_w is integrated over the star's lifetime to determine the total kinetic energy injected by its winds into the ISM.

Figure 9 illustrates v_∞ and L_w of $25 M_\odot$ stars with different Z values around Z_c . Main-sequence O stars produce fast winds of $\sim 1500\text{--}3000 \text{ km s}^{-1}$. When a star evolves into an RSG, its v_∞ suddenly drops by a factor of 100. At the same time, its \dot{M} goes up by 2–3 orders of magnitude (Figure 7). As a result, L_w decreases by 1–2 orders of magnitude when the star evolves from a main-sequence O star to an RSG. Although cool RSG winds release large amounts of mass, they only carry relatively small amounts of kinetic energy because of their slow wind velocities. For stars with higher initial masses and metallicities, the domination of hot winds in the energy output is even more significant.

Figure 10 presents the total kinetic energy output over the stellar lifetime of each model. This figure also shows the contributions of the hot and cool winds separately. It is evident that the hot winds dominate the energy output, while the contributions from cool winds are almost negligible. The dominance of hot winds is attributed to their velocities being much faster than the cool winds' velocities, and their duration (including the main-sequence stage) spanning $\sim 90\%$ of the stellar lifetime. It can also be seen from the top panel of Figure 10 that the most massive stars with near-solar metallicities each inject $10^{50}\text{--}10^{51}$ erg of kinetic energy into the

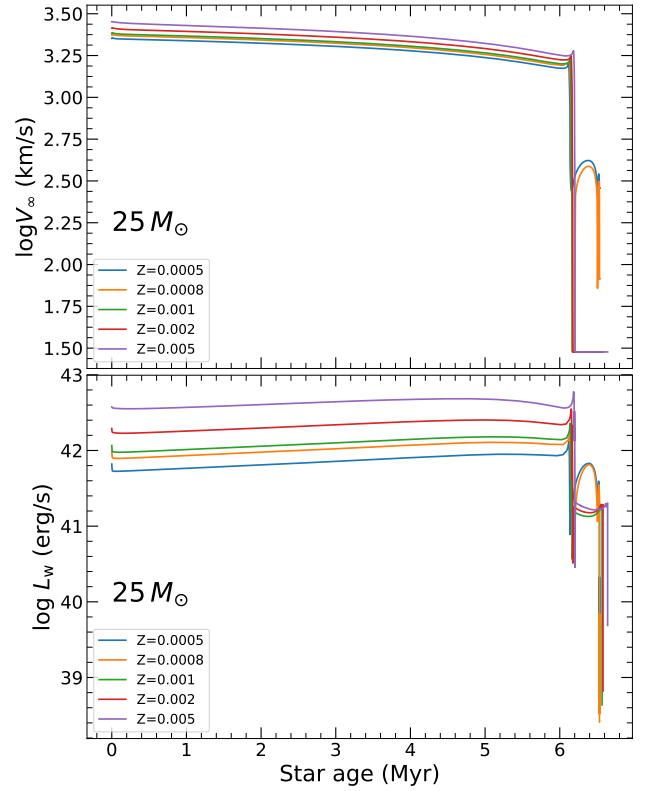


Figure 9. The evolution of wind terminal velocity v_∞ (*top panel*) and mechanical luminosity L_w (*bottom panel*) of stars with initial mass $25 M_\odot$ and different metallicities near Z_c . Sudden transitions of v_∞ and L_w occur when the stars enter the post-main-sequence stage after the age of 6 Myr.

surrounding ISM, which is comparable to the explosion energy of a SN. In contrast, the cool winds of such a massive star contribute only up to $\sim 10^{47}$ erg to the total kinetic energy.

It is interesting to note that the Z_c for the dichotomy of total mass loss show some effects only the cool winds' total kinetic energy. This is understandable because Z_c is closely associated with the onset of cool winds, as discussed in Section 4.3. The stellar winds' total kinetic energy injected into the ISM is dominated by contributions from hot winds. As cool winds play a negligible role in the total wind energy, its closely associated Z_c does not affect the total wind energy or total hot wind energy. In other words, whether a star becomes an RSG has no bearing on the total wind kinetic energy injected to the ISM.

5.2. Wind Feedback from a Star Cluster

The mass loss and kinetic energy output from stellar winds of individual stars can be used to evaluate the feedback from a star cluster. We consider a star cluster from a single burst of star formation with an initial mass function (IMF) $\xi(M) = \xi_0 M^{-\alpha}$, where M is the initial stellar mass, ξ_0 is a scaling factor, and α is a constant. Here, ξ_0 is scaled by the number of stars in the system N so that $dN = \xi_0 M^{-\alpha} dM$. In our calculations, we apply $\alpha = 2.35$ (the Salpeter IMF; Salpeter 1955). For comparison, the widely used IMF in Kroupa (2001) gives $\alpha = 2.3$ for stars with masses $> 1 M_\odot$, which is similar to the Salpeter IMF.

We have calculated the feedback for a cluster with a total mass of $10^5 M_\odot$. Although this mass is associated with a super star cluster, the feedback scales linearly with the cluster mass and can be used to determine feedback of clusters of any other masses. For the cluster members, we adopt the canonical initial stellar mass range of $1 - 150 M_\odot$. We note that the upper mass limit is not important because the population of very massive stars is much smaller than that of lower-mass stars. With the above assumptions, we integrate the \dot{M} and L_w of individual stars to calculate the wind feedback from the entire cluster. The feedback we present only include the contributions from massive stars of $M_i = 11 - 60 M_\odot$, which is the mass range of our simulations; thus, our results show the lower limit of wind feedback.

In Figure 11, we choose a high- Z ($Z = 0.02$) case and a low- Z ($Z = 0.0002$) case and plot their integrated mass-loss rates and energy-injection rates of a $10^5 M_\odot$ cluster before the age of 10 Myr. At about 3–4 Myr, the most massive stars evolve into the post-main-sequence stage. In the high- Z cluster, these massive stars successively become cool supergiants and significantly enhance the overall mass-loss rate. However, the lifetimes of cool supergiants are short, so each star can only contribute to the enhancement of mass-loss rate for a short time. When stars of lower masses become cool supergiants, the more massive stars have already ended their lifetimes. The overall trend of the mass-loss rate is a gradual decrease after the sudden enhancement at about 3–4 Myr. The jagged appearance of the curve of mass-loss rate is caused by

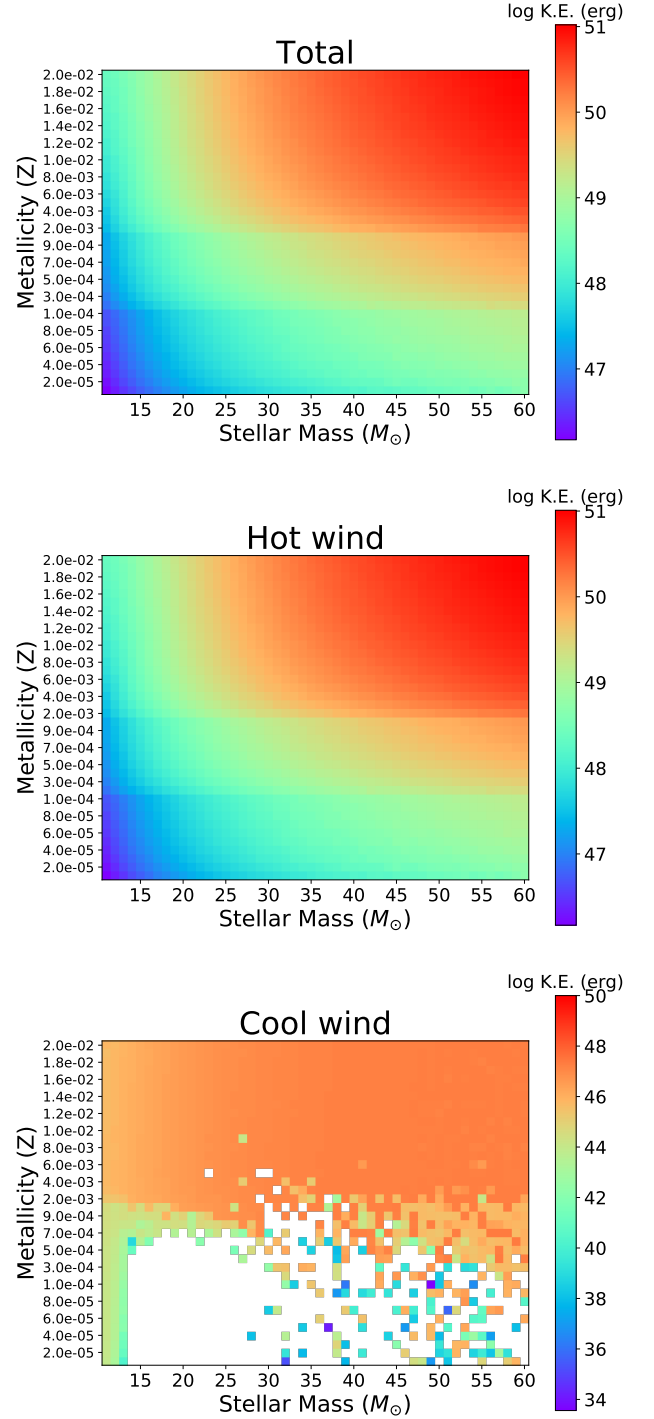


Figure 10. The total kinetic energy released by stellar winds throughout the stellar lifetimes. Each pixel in this map represents a stellar model. Note that the y-axis scale is non-uniform. In addition to the total energy, we separately plot the contributions from hot and cool winds, and hot winds dominate the kinetic energy released by stellar winds.

the limit of mass resolution ($1 M_\odot$) in our simulations. For the low- Z cluster, the stars do not evolve into cool supergiants

at the helium-core burning stage, so the mass-loss rate after 4 Myr can only increase to $10^{-5} M_{\odot}/\text{yr}$ due to the bi-stability jumps. Some sudden spikes of mass-loss rate occur at about 4 Myr because some low- Z stars reach cool supergiants in the very late stage of their lifetimes, and thus they have enhanced the mass-loss rate for very short times.

While the mass-loss rate of the high- Z cluster is enhanced by cool winds at the ages of 3–4 Myr, cool winds do not contribute much to the energy injection rate. Thus, for both high- and low- Z clusters, their energy injection rates do not rise drastically but continue to decline after 3–4 Myr, when the most massive stars end their lifetimes.

We compare our mass-loss rates and energy injection rates with those adopted by the FIRE-3 cosmological simulations (Hopkins et al. 2022), which are shown by the blue dash lines in Figure 11. The mass-loss rate in FIRE-3 is expressed by a function of time and Z with four segments separated by 1.7, 4, and 20 Myr. For the high- Z model, the post-main-sequence mass-loss rate from our simulations is in reasonable agreement with the FIRE-3 curve, while for the low- Z model, our mass-loss rate after ~ 4 Myr is about one order of magnitude lower than the FIRE-3 rate. The essential difference is because the low- Z stars in our models do not evolve into cool supergiants when they enter the post-main-sequence stage, so the mass-loss rate is low. For the times before 4 Myr, the comparison of mass-loss rates is out of our scope as we do not consider the very massive stars with $> 60 M_{\odot}$. We also compare our energy injection rate the FIRE-3 function. For both high- and low- Z cases, our energy injection rate is lower than the FIRE-3 rate by about a order of magnitude after ~ 4 Myr. FIRE-3 uses the entire mass-loss rate and the average velocity, which is $\sim 1,000 \text{ km s}^{-1}$ at ~ 4 Myr, to estimate the wind feedback. In contrast, we separately consider hot and cool winds, with hot winds having velocities of $> 1,000 \text{ km s}^{-1}$ but low mass-loss rates and cool winds having high mass-loss rates but a velocity of 30 km s^{-1} . Thus, our calculations lead to a lower energy injection rate than the FIRE-3 function.

We have calculated the feedback from stellar winds in a cluster using the Salpeter IMF. The critical metallicity of cool supergiant formation significantly affects the total mass loss within a cluster, and we suggest that this effect be considered in order to refine the treatment of stellar feedback in cosmological simulations. In contrast, the kinetic energy feedback is dominated by hot winds, which are irrelevant to the critical metallicity of cool supergiants.

We further integrate the mass and energy injected by a $10^5 M_{\odot}$ cluster over time, and the results are shown in Figure 12. The contribution of wind feedback in our calculations is from star with $M_1 = 11 - 60 M_{\odot}$. For comparison, we also plot the feedback that only includes the contribution of 11–30 M_{\odot} stars. From these plots, hot winds dominate the kinetic

energy and momentum feedback for all of the metallicities, while the cool winds surpasses hot winds in the contribution to mass loss when $Z > Z_c$. The effect of critical metallicity occurs in the output of mass, but not in that of kinetic energy. The WR wind is never the dominating component, although its contribution to kinetic energy is larger than cool wind in an environment of solar metallicity. We note that these integrated quantities are the lower limit, as we do not consider the very massive stars with $> 60 M_{\odot}$.

6. DISCUSSIONS

This section discusses some implications of and remaining issues with our results. In Section 6.1, we discuss the effects of metallicity on cool supergiant evolution. In Section 6.2, we point out the possible uncertainties in our models. Finally, in Section 6.3, we discuss the implications of critical metallicity on the fates and environments of massive stars.

6.1. Two Effects of Metallicity on RSG Evolution

Our study finds that the critical metallicity of cool supergiant formation causes a significant increase in mass loss. This effect arises from stellar evolution rather than the treatment of mass-loss prescription. We discern two different effects of metallicity on RSG evolution and review the previous theoretical works that have shown a similar result of critical metallicity.

From the evolutionary tracks shown in Figure 7, there are two apparent effects of metallicity on the evolution of cool supergiants. First, at a lower metallicity, the overall evolutionary tracks, from the ZAMS to the supergiant stage, shift to higher T_{eff} or bluer locations. Second, the evolutionary tracks of stars with $Z < Z_c$ end at hotter T_{eff} , whereas stars with $Z > Z_c$ can successfully evolve into cooler regimes. This is a sharp transition rather than a continuous change. In the following paragraphs we discuss these two different effects.

(1) *The overall shift of the evolutionary tracks with metallicity.* This effect has been discussed with regard to the two ends of stellar evolution: the shift of ZAMS and the color of supergiants. First, the displacement of ZAMS toward the bluer locations with decreasing Z has been reported by stellar models (e.g., Schaller et al. 1992; Mowlavi et al. 1998; Groh et al. 2019). Among several physical parameters that directly change with metallicity (opacity, energy generation rate, molecular weight, etc.), the ZAMS shift has been attributed to opacity κ (see e.g., Maeder 2009). In general, decreasing Z leads to lower κ , transferring more radiation outward and leading to higher luminosities, and the stars also need to contract further to maintain the energetic equilibrium. With a larger L and a smaller R , a higher $T_{\text{eff}} (\propto L/R^2)$ is required for lower- Z stars.

At the end of stellar evolution, supergiants with lower Z also shift toward bluer locations in the HR diagram. This feature has been observed in stars in the local group (Humphreys

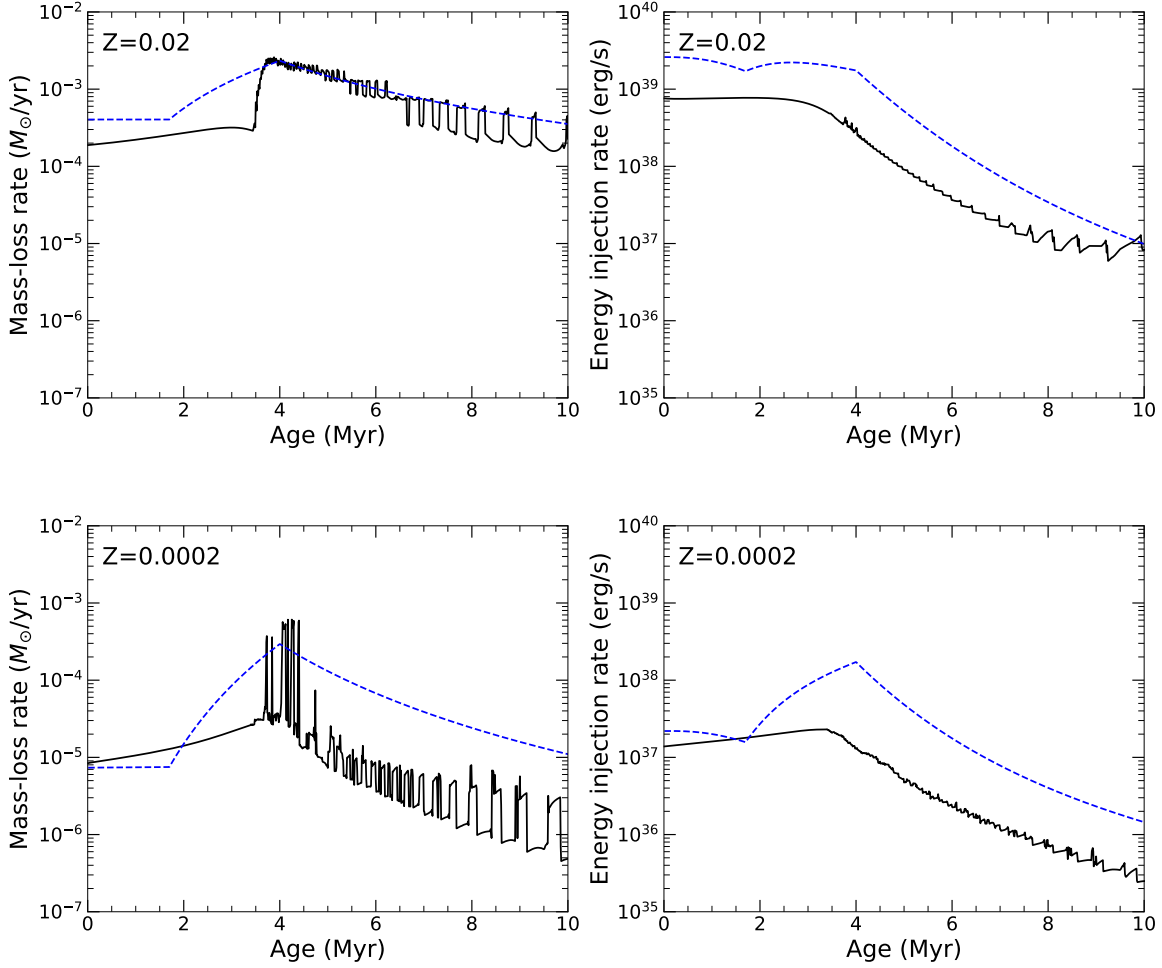


Figure 11. The integrated mass-loss rate and energy-injection rate from stellar winds in a star cluster of $10^5 M_{\odot}$, in which the Salpeter IMF is assumed. The upper and lower panels show the results of a $Z = 0.02$ cluster and a $Z = 0.0002$ cluster, respectively. The blue dash lines show the functions adopted in the feedback treatment of the FIRE-3 cosmological simulation (Hopkins et al. 2022).

1979a,b; Elias et al. 1985), and has been reproduced in stellar models (e.g., Schaller et al. 1992; Meynet et al. 1994; Groh et al. 2019). Surveys of massive stars have confirmed that the RSGs in galaxies with lower metallicities have earlier spectral types on average: M2 I in the Milky Way, M1-M1.5 I in the LMC, and K3-K7 I in the Small Magellanic Cloud (SMC) (Massey & Olsen 2003; Levesque et al. 2006). This can be explained as the shift of the Hayashi line, which represents the coolest extent of giant stars, to higher T_{eff} at lower Z (Elias et al. 1985; Levesque et al. 2006). These stars shift to bluer positions at lower Z due to opacity (Hayashi & Hoshi 1961; Kippenhahn et al. 2012), which is a similar physical effect to the ZAMS shift.

(2) *The critical metallicity of cool supergiant formation.* Instead of causing continuous shifts in the HR diagram, the critical metallicity acts as a boundary between two different types of evolution tracks in the supergiant stage. The stars with $Z > Z_c$ successfully become RSG with $R \gtrsim 1,000 R_{\odot}$,

and those with $Z < Z_c$ remain as smaller BSGs. This effect causes the significant increase in mass loss.

Some previous models have shown that low- Z stars can never evolve into RSGs (Arnett 1991; Baraffe & El Eid 1991; Brocato & Castellani 1993; Hirschi 2007; El Eid et al. 2009; Limongi 2017; Groh et al. 2019). The metallicity value has been identified as $Z \sim 10^{-3}$ (Baraffe & El Eid 1991; El Eid et al. 2009), which is consistent with our results. We start from the investigation of mass loss and identify the same phenomenon in cool supergiant formation.

However, the physical origin of the critical metallicity of cool supergiant formation is still poorly understood. A profound question remains: Why do massive stars of $Z > Z_c$ successfully expand to RSGs, but those of $Z < Z_c$ fail to become RSGs? In companion Paper II, we will present some experiments that study the physical origin of critical metallicity. The explanation of its mechanism will help us understand the fundamental physics of RSG formation.

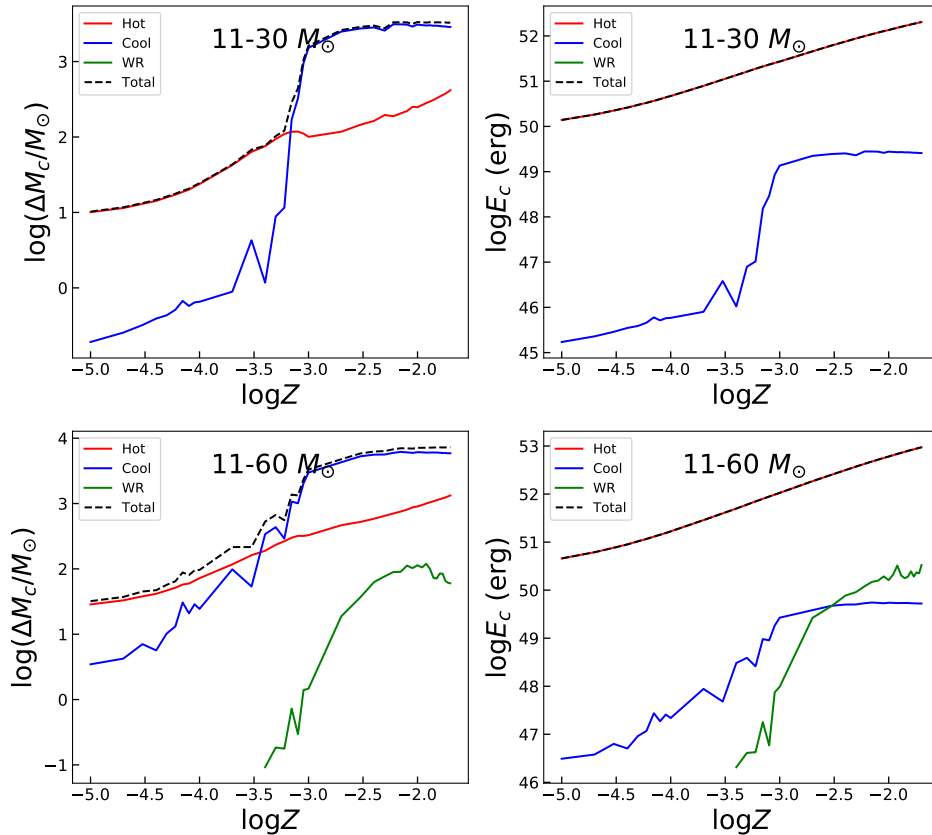


Figure 12. The mass (left panels) and kinetic energy (right panels) released by the stellar winds in a star cluster of $10^5 M_{\odot}$, in which the Salpeter IMF is assumed. The upper panels only include the contribution from stars of 11–30 M_{\odot} , and the lower panels include the effect from all of our models within 11–60 M_{\odot} . The curves of mass loss show a significant increase around the critical metallicity of ($Z \sim 10^{-3}$), where the cool winds exceed the hot winds. The corresponding kinetic energy curves are dominated by hot winds and thus do not show any sudden increase around the critical metallicity.

6.2. Possible Uncertainties

In this subsection, we discuss the uncertainties in our models from both stellar models and mass-loss prescriptions. We then evaluate the impacts of these factors on our main results.

6.2.1. Uncertainties from stellar models

For simplicity, this work only considers single and non-rotating stars. In fact, many recent studies of stellar evolution consider the effects of rotation and binarity (e.g., Langer 2012, for review).

Stellar rotation can change the evolution tracks through processes such as rotational mixing (Maeder 2009). For RSGs, rotation is suggested to prevent a large intermediate convective zone, thus preventing the star from evolving backward to the blue side (Maeder 2009). It has also been suggested that at low metallicities, evolving into RSGs is easier for rotating stars than for non-rotating stars (Hirschi 2007).

Binarity is another important factor in recent stellar evolution studies, as most massive stars are found in binaries (Sana et al. 2012; Duchêne, & Kraus 2013). Mass transfer is one of the essential processes in interacting binary stars

that dramatically changes the post-main-sequence evolution (e.g., Iben 1991; Taam & Sandquist 2000; Yoon et al. 2010; Langer 2012; Smith 2014). For example, an RSG can strip off its envelope due to mass transfer and move back to bluer locations in the HR diagram, becoming a YSG or WR star (Levesque 2017).

Therefore, for rotating and binary stars, we cannot presume that the feature of critical metallicity is the same as our results of non-rotating and single stars. Furthermore, internal mixing processes such as semiconvection and overshooting can affect the evolution of supergiants (Schootemeijer et al. 2019), and thus they may impact the critical metallicity. The effects of rotation, binarity, and mixing processes on cool supergiant formation and the corresponding mass loss are thus worth studying in future works.

Another minor issue in our model is that some models of 11–17 M_{\odot} do not successfully run until the iron core collapses. Instead, they stall at the carbon or oxygen burning stage. This situation does not affect our results, as the criterion of high or low mass loss refers to whether a star becomes a cool supergiant at the beginning of the core-helium burning

stage. The final evolutionary stages only last for a very short time and thus do not contribute any significant mass loss via steady-state winds. Moreover, the models of $>17 M_{\odot}$, which smoothly evolve until the iron core collapses, already unambiguously demonstrate the feature of critical metallicity.

We further point out the limits of 1D stellar evolution models. First, mixing in a 1D stellar model is done through the mixing length theory, which assumes all the chemical elements homogeneously mix together within the local pressure scale height if fluid instabilities occur. However, the mixing length theory likely becomes invalid inside the shell-burning region where violent burning, dynamics, and nucleosynthesis coevolve. Precise mixing then becomes challenging. Since a full 3D stellar evolution model is still unavailable, recent efforts (Trampedach et al. 2013, 2014a,b; Jørgensen et al. 2018; Mosumgaard et al. 2018) have started to use local or global 3D hydro simulations of stellar convective zones to physically calibrate the parameters of mixing length theory used in 1D stellar evolution models.

Another critical issue is the opacities of the stellar atmosphere. One-dimensional stellar evolution models of MESA primarily focus on interior nuclear burning and structure evolution, and their stellar envelopes contain numerical artifacts due to their poor resolution in the Lagrangian code. In addition, the gas in the stellar atmosphere is at non-local thermal equilibrium, and its ionization states are difficult to calculate correctly. These issues can alter the surface opacities and significantly affect the physical properties of wind. Solving this problem requires multi-D radiation-hydro simulations, including sophisticated atomic physics, to evolve the wind using the first principles.

6.2.2. Uncertainties from mass-loss prescriptions

The currently available mass-loss prescriptions are based on the fitting of data obtained from simulations or observations, as described in Section 2. The best-effort prescriptions remain uncertain, and various prescriptions have been proposed. A comprehensive review of these prescriptions was given by Maeron & Josselin (2011). More recently, some new prescriptions have been proposed for hot winds (e.g., Björklund et al. 2022) and cool winds (e.g., Goldman et al. 2017; Beasor et al. 2020). A new study of RSG mass loss by Beasor et al. (2020) suggested that dJ88 overestimated the mass-loss rate by a factor of nine.

To explore the impact of uncertain mass-loss rates on stellar evolution, Renzo et al. (2017) performed a grid of stellar evolution simulations with MESA using different wind prescriptions. They also re-scaled the wind prescriptions by multiplying the mass-loss rates by a wind efficiency parameter η and carried out simulations using η of 0.1, 0.33, and 1. They found $\sim 50\%$ variations in the final stellar mass within

all the combinations of η and wind prescriptions and $\sim 15\text{--}30\%$ changes in the final stellar mass for a fixed $\eta = 1$.

Another limit in our study is that we only consider steady-state winds. In addition to steady-state winds, the LBVs have eruptive mass loss driven by super-Eddington winds (Humphreys, & Davidson 1994; Shaviv 2000; Smith & Owocki 2006; Owocki et al. 2017; Vink 2018; Owocki et al. 2019), such as η Carinae. These eruptive LBV winds may be a promising source of metal enrichment for Pop III stars in the early universe (Smith & Owocki 2006).

The physical properties of a star cluster can also affect the mass loss of its resident stars. For example, in a cluster with multiple stellar populations, as a new star starts to form in the dense stellar environment shaped by the old stars, the accretion disk of its proto-star is disrupted by the gravity of old stars, leading to the formation of a rapidly rotating star that evolves longer during its red giant phase, and produce more mass loss (Tailo et al. 2015, 2020, 2021). Although this environmental effect is based on the low-mass stars, we speculate that it may apply to forming massive stars and altering their mass loss.

The extension of the mass-loss prescriptions to low metallicities is another issue. For hot winds, Vink et al. (2001) compared their mass-loss prescription with observations of stars in the SMC, where $Z \sim 1/5 Z_{\odot}$, and found reasonable agreement. It has been suggested that at $Z \sim 1/7 Z_{\odot}$ mass-loss rates derived from non-LTE stellar atmospheric model fittings of the optical spectra cannot be described by the V01's prescription (Tramper et al. 2011; Tramper 2014). Nonetheless, subsequent analyses of far-UV spectra of the same targets indicate that Tramper et al. (2011)'s low-Z stars actually have metallicities $\sim 1/5 Z_{\odot}$, making the mass-loss rates consistent with V01's prescription (Bouret et al. 2015). In regards to the cool winds, dJ88's prescription has also been tested in the SMC (Maeron & Josselin 2011). Generally speaking, the mass-loss prescriptions have been tested in low-Z stars with $Z \sim 1/5 Z_{\odot}$. For even lower metallicities, it is not known whether any breakdown of these scaling relations occurs. Few extremely metal-poor stars have been observed, and most of them are low-mass stars (Beers, & Christlieb 2005; Yong et al. 2013; Da Costa et al. 2019), thus yielding no information on the mass-loss rates of massive stars. For now, adopting the widely-used mass-loss prescriptions in low-Z regimes is the only feasible method.

It is also unclear what kind of Z-dependent function should be included in mass-loss rate, as uncertainty exists, especially for cool winds. Earlier prescriptions of cool winds do not include the Z-dependence (de Jager et al. 1988; Nieuwenhuijzen & de Jager 1990; van Loon et al. 2005), but some later works adopt $\dot{M} \sim Z^m$ in their simulations (e.g., Maeron & Josselin 2011; Groh et al. 2019). Nevertheless, some recent observations show that mass-loss rates of RSGs are

nearly independent of Z (Goldman et al. 2017; Beasor et al. 2020). We use the conventional dJ88 prescription without Z -dependence, but are aware of uncertainties in this function.

Fortunately, most of these uncertain factors in mass-loss prescriptions only slightly affect our main results. The major difference in mass loss between high- and low- Z stars depends on whether a star evolves into the RSG phase rather than the mass-loss prescriptions. In other words, the physical origin of the critical metallicity lies in stellar evolution, regardless of the adopted recipe of mass loss, although these two processes can couple together to some extent. We carried out a simple test and found that even if the mass loss is fully turned off, the critical metallicity of cool supergiant formation still exists. As long as the mass-loss rate in the RSG phase is much higher than that in the main-sequence phase, the critical metallicity of cool supergiant formation leads to the bimodal distribution of mass loss. Therefore, whether the mass-loss rate is a function of $\dot{M} \sim Z^m$ is only a minor issue.

6.3. Implications of the Critical Metallicity

Our study reveals a critical metallicity of cool supergiant formation that leads to a significant difference in mass loss between high- and low- Z environments. The low- Z stars do not evolve into cool supergiants, and thus only have minimal mass loss through steady-state winds over their lifetimes. In the following paragraphs, we discuss the consequences of the critical metallicity.

It is widely known that pre-SN evolution and mass loss set up the physical condition for SN explosions. The types of progenitor stars often determine the types of SNe. For example, RSGs are the progenitors of SNe II-P, as identified in pre-SN images (Smarrt 2009, 2015, for review). It has also been shown that the types of SNe can be significantly affected by the interaction with CSM produced by RSGs (e.g., van Loon 2010; Ekström et al. 2012; Smith 2014; Smarrt 2015; Beasor et al. 2020, 2021; Moriya 2021). For example, the early-phase light curves of SNe II-P can be better explained if dense CSM is considered (Moriya et al. 2011, 2017, 2018). Moreover, it is suggested that CSM not only affects SN types but also makes SN explosions more likely to happen (Morozova et al. 2018).

Based on these understandings and the critical metallicity we found, we can expect the low- Z stars to behave differently from high- Z stars in SN explosions. First, if the low- Z stars indeed end up as BSGs instead of RSGs, whether they will still explode as SNe is uncertain. Even if they successfully explode, the resulting SN type may differ from SNe II-P. Low- Z stars never go through the RSG phase, or only become RSGs in the very final stage, so they only lose a negligible amount of mass and may not end as typical SNe II-P. Their circumstellar material can be too dilute for interacting

SNe, although we have not considered eruptive mass loss that can generate dense CSM.

On a larger scale, the critical metallicity also impacts the stellar feedback in a star cluster. From our results, the total mass returned to the ISM by stellar winds shows a significant increase at Z_c . In the high- Z ($Z > Z_c$) domain, these results are consistent with the current treatment of feedback in cosmological simulations such as FIRE-3. However, if the low- Z ($Z < Z_c$) stars do not evolve into cool supergiants, as our simulations predict, the current treatment of feedback may overestimate the mass injected to the ISM in these low- Z environments. This discrepancy exists only in mass injection but not in energy output, as the kinetic energy feedback is dominated by hot winds, which are irrelevant to the critical metallicity.

As the critical metallicity $Z_c \sim 0.001$ is lower than $0.1 Z_\odot$, it is still difficult to test it using current observational instruments. Nevertheless, it will be promising to test the stellar evolution below this metallicity with the next-generation telescopes. For example, observations of massive stars in the low- Z galaxies are listed as one of the scientific goals of the LUVVOIR observatory (Garcia et al. 2019).

In future works, we plan to apply these 1D mass loss models to 2D and 3D radiation hydro simulations to further understand how the mass loss shapes the CSM and ISM around massive stars. With the advancement of numerical models and observational data, we may reveal the mystery of the mass loss of massive stars and their feedback.

7. CONCLUSIONS

We studied the total mass loss of massive stars and their dependence on metallicity by performing 1D stellar evolution simulations with MESA. In the initial mass range $11\text{--}60 M_\odot$, the total mass loss increases dramatically if their metallicity becomes higher than $Z \sim 10^{-3}$. We call this *critical metallicity*, though the exact metallicity values for this mass-loss jump are not very well defined. Cool winds that operate in the cool supergiant phase are responsible for this mass-loss jump. Massive stars with $Z < Z_c$ usually stay blue during the post-main sequence; thus, the cool winds are not operating, and the mass loss is low. In contrast, massive stars with $Z > Z_c$ successfully become cool supergiants, leading to significantly higher mass loss. The critical metallicity of cool supergiant formation gives rise to the bimodal distribution of mass loss.

We also calculated the feedback of stellar winds in a star cluster. In low- Z environments, we may overestimate the integrated mass loss in a cluster if we do not consider the effect of critical metallicity. While the mass loss of a cool supergiant is much higher than that of a hot main-sequence star, its wind velocity is much lower, so its kinetic energy output

is lower. Consequently, the critical metallicity affects mass loss but not kinetic energy feedback.

In summary, we identified the critical metallicity of cool supergiant formation in our stellar models. A striking consequence of the critical metallicity is the significant jump in mass loss when we adopt the widely used wind prescriptions. This evolutionary effect may have various consequences on the fates of metal-poor stars in the early universe.

¹ This research is supported by the Ministry of Science and
² Technology, Taiwan under grant no. MOST 110-2112-M-
³ 001-068-MY3 and the Academia Sinica, Taiwan under a ca-
⁴ reer development award under grant no. AS-CDA-111-M04.

REFERENCES

- Abbott, D. C., & Lucy, L. B. 1985, *ApJ*, 288, 679
- Abbott, D. C. 1982, *ApJ*, 263, 723
- Agertz, O., & Kravtsov, A. V. 2015, *ApJ*, 804, 18
- Arnett, D. 1991, *ApJ*, 383, 295. doi:10.1086/170786
- Arnett, W. D., Bahcall, J. N., Kirshner, R. P., et al. 1989, *ARA&A*, 27, 629. doi:10.1146/annurev.aa.27.090189.003213
- Asplund, M., Grevesse, N., Sauval, A. J., et al. 2009, *ARA&A*, 47, 481
- Baraffe, I. & El Eid, M. F. 1991, *A&A*, 245, 548
- Beasor, E. R., Davies, B., & Smith, N. 2021, *ApJ*, 922, 55. doi:10.3847/1538-4357/ac2574
- Beasor, E. R., Davies, B., Smith, N., et al. 2020, *MNRAS*, 492, 5994. doi:10.1093/mnras/staa255
- Beasor, E. R., & Davies, B. 2018, *MNRAS*, 475, 55
- Björklund, R., Sundqvist, J. O., Singh, S. M., et al. 2022, arXiv:2203.08218
- Beers, T. C., & Christlieb, N. 2005, *ARA&A*, 43, 531
- Bouret, J.-C., Lanz, T., Hillier, D. J., et al. 2015, *MNRAS*, 449, 1545
- Brocato, E. & Castellani, V. 1993, *ApJ*, 410, 99. doi:10.1086/172729
- Castor, J. I. 1993, *Massive Stars: Their Lives in the Interstellar Medium*, 35, 297
- Castor, J. I., Abbott, D. C., & Klein, R. I. 1975, *ApJ*, 195, 157
- Chen, K.-J., Woosley, S. E., & Whalen, D. J. 2020, *ApJ*, 893, 99. doi:10.3847/1538-4357/ab7db0
- Choi, J., Dotter, A., Conroy, C., et al. 2016, *ApJ*, 823, 102. doi:10.3847/0004-637X/823/2/102
- Chu, Y.-H. 2008, *Massive Stars as Cosmic Engines*, 250, 341. doi:10.1017/S1743921308020681
- Da Costa, G. S., Bessell, M. S., Mackey, A. D., et al. 2019, *MNRAS*, 489, 5900
- Dale, J. E. 2015, *NewAR*, 68, 1
- Decin, L. 2021, *ARA&A*, 59, 337. doi:10.1146/annurev-astro-090120-033712
- de Jager, C., Nieuwenhuijzen, H., & van der Hucht, K. A. 1988, *A&AS*, 72, 259
- Duchêne, G., & Kraus, A. 2013, *ARA&A*, 51, 269
- Dwarkadas, V. V. 2005, *ApJ*, 630, 892
- Ekström, S., Georgy, C., Eggenberger, P., et al. 2012, *A&A*, 537, A146. doi:10.1051/0004-6361/201117751
- El Eid, M. F., The, L.-S., & Meyer, B. S. 2009, *SSRv*, 147, 1. doi:10.1007/s11214-009-9517-6
- Elias, J. H., Frogel, J. A., & Humphreys, R. M. 1985, *ApJS*, 57, 91. doi:10.1086/190997
- Emerick, A., Bryan, G. L., & Mac Low, M.-M. 2019, *MNRAS*, 482, 1304
- Fichtner, Y. A., Grassitelli, L., Romano-Díaz, E., et al. 2022, *MNRAS*. doi:10.1093/mnras/stac785
- Fierlinger, K. M., Burkert, A., Ntormousi, E., et al. 2016, *MNRAS*, 456, 710
- Freyer, T., Hensler, G., & Yorke, H. W. 2003, *ApJ*, 594, 888
- Garcia, M., Evans, C. J., Bestenlehner, J. M., et al. 2019, arXiv:1908.04687
- Georgy, C. 2012, *A&A*, 538, L8
- Goldman, S. R., van Loon, J. T., Zijlstra, A. A., et al. 2017, *MNRAS*, 465, 403
- Groh, J. H., Ekström, S., Georgy, C., et al. 2019, *A&A*, 627, A24
- Hayashi, C. & Hoshi, R. 1961, *PASJ*, 13, 442
- Henry, L., Vardya, M. S., & Bodenheimer, P. 1965, *ApJ*, 142, 841
- Hirschi, R. 2007, *A&A*, 461, 571
- Hopkins, P. F., Wetzel, A., Wheeler, C., et al. 2022, arXiv:2203.00040
- Hopkins, P. F., Wetzel, A., Kereš, D., et al. 2018, *MNRAS*, 480, 800
- Hopkins, P. F., Kereš, D., Oñorbe, J., et al. 2014, *MNRAS*, 445, 581
- Humphreys, R. M., Helmelt, G., Jones, T. J., et al. 2020, *AJ*, 160, 145. doi:10.3847/1538-3881/abab15
- Humphreys, R. M., & Davidson, K. 1994, *PASP*, 106, 1025
- Humphreys, R. M. 1979, *ApJS*, 39, 389. doi:10.1086/190578
- Humphreys, R. M. 1979, *ApJ*, 231, 384. doi:10.1086/157201
- Iben, I. 1991, *ApJS*, 76, 55. doi:10.1086/191565
- Iglesias, C. A., & Rogers, F. J. 1996, *ApJ*, 464, 943
- Jørgensen, A. C. S., Mosumgaard, J. R., Weiss, A., et al. 2018, *MNRAS*, 481, L35. doi:10.1093/mnras/sly152
- Kippenhahn, R., Weigert, A., & Weiss, A. 2012, *Stellar Structure and Evolution*. ISBN: 978-3-642-30304-3. Berlin, Heidelberg: Springer Berlin Heidelberg, 2012.. doi:10.1007/978-3-642-30304-3
- Krause, M., Fierlinger, K., Diehl, R., et al. 2013, *A&A*, 550, A49
- Kroupa, P. 2001, *MNRAS*, 322, 231. doi:10.1046/j.1365-8711.2001.04022.x
- Lamers, H. J. G. L. M., Snow, T. P., & Lindholm, D. M. 1995, *ApJ*, 455, 269. doi:10.1086/176575
- Langer, N. 2012, *ARA&A*, 50, 107
- Leitherer, C., Robert, C., & Drissen, L. 1992, *ApJ*, 401, 596
- Levesque, E. M. 2017, *Astrophysics of Red Supergiants*, by Levesque, Emily M.. ISBN: 978-0-7503-1329-2. IOP ebooks. Bristol, UK: IOP Publishing, 2017. doi:10.1088/978-0-7503-1329-2
- Levesque, E. M., Massey, P., Olsen, K. A. G., et al. 2006, *ApJ*, 645, 1102. doi:10.1086/504417
- Limongi, M. 2017, *Handbook of Supernovae*, 513
- Lucy, L. B., & Solomon, P. M. 1970, *ApJ*, 159, 879
- Maeda, K., Hattori, T., Milisavljevic, D., et al. 2015, *ApJ*, 807, 35

- Maeder, A. 2009, *Physics, Formation and Evolution of Rotating Stars*, Astronomy and Astrophysics Library. ISBN 978-3-540-76948-4. Springer Berlin Heidelberg, 2009.
doi:10.1007/978-3-540-76949-1
- Marinacci, F., Sales, L. V., Vogelsberger, M., et al. 2019, *MNRAS*, 489, 4233
- Massey, P. & Olsen, K. A. G. 2003, *AJ*, 126, 2867.
doi:10.1086/379558
- Mauron, N., & Josselin, E. 2011, *A&A*, 526, A156
- McCray, R. & Fransson, C. 2016, *ARA&A*, 54, 19.
doi:10.1146/annurev-astro-082615-105405
- Meynet, G., Maeder, A., Schaller, G., et al. 1994, *A&AS*, 103, 97
- Mokiem, M. R., de Koter, A., Vink, J. S., et al. 2007, *A&A*, 473, 603
- Moriya, T. J. 2021, *MNRAS*, 503, L28.
doi:10.1093/mnras/lsab018
- Moriya, T. J., Förster, F., Yoon, S.-C., et al. 2018, *MNRAS*, 476, 2840. doi:10.1093/mnras/sty475
- Moriya, T. J., Yoon, S.-C., Gräfenor, G., & Blinnikov, S. I. 2017, *MNRAS*, 469, L108
- Moriya, T., Tominaga, N., Blinnikov, S. I., et al. 2011, *MNRAS*, 415, 199. doi:10.1111/j.1365-2966.2011.18689.x
- Morozova, V., Piro, A. L., & Valenti, S. 2018, *ApJ*, 858, 15.
doi:10.3847/1538-4357/aab9a6
- Mosumgaard, J. R., Ball, W. H., Silva Aguirre, V., et al. 2018, *MNRAS*, 478, 5650. doi:10.1093/mnras/sty1442
- Mowlavi, N., Meynet, G., Maeder, A., et al. 1998, *A&A*, 335, 573
- Nieuwenhuijzen, H. & de Jager, C. 1990, *A&A*, 231, 134
- Nugis, T., & Lamers, H. J. G. L. M. 2002, *A&A*, 389, 162
- Nugis, T., & Lamers, H. J. G. L. M. 2000, *A&A*, 360, 227
- O'Connor, E., & Ott, C. D. 2011, *ApJ*, 730, 70
- Ou, P.-S., Chu, Y.-H., Maggi, P., et al. 2018, *ApJ*, 863, 137
- Owocki, S. P., Hirai, R., Podsiadlowski, P., et al. 2019, *MNRAS*, 485, 988. doi:10.1093/mnras/stz461
- Owocki, S. P., Townsend, R. H. D., & Quataert, E. 2017, *MNRAS*, 472, 3749
- Pauldrach, A. W. A., & Puls, J. 1990, *A&A*, 237, 409
- Patnaude, D. J., Lee, S.-H., Slane, P. O., et al. 2017, *ApJ*, 849, 109
- Paxton, B., Smolec, R., Schwab, J., et al. 2019, *ApJS*, 243, 10
- Paxton, B., Schwab, J., Bauer, E. B., et al. 2018, *ApJS*, 234, 34
- Paxton, B., Marchant, P., Schwab, J., et al. 2015, *ApJS*, 220, 15
- Paxton, B., Cantiello, M., Arras, P., et al. 2013, *ApJS*, 208, 4
- Paxton, B., Bildsten, L., Dotter, A., et al. 2011, *ApJS*, 192, 3
- Pillepich, A., Springel, V., Nelson, D., et al. 2018, *MNRAS*, 473, 4077
- Puls, J., Vink, J. S., & Najarro, F. 2008, *A&A Rv*, 16, 209
- Reimers, D. 1975, *Memoires of the Societe Royale des Sciences de Liege*, 8, 369
- Renzo, M., Ott, C. D., Shore, S. N., & de Mink, S. E. 2017, *A&A*, 603, A118
- Rey-Raposo, R., Dobbs, C., Agertz, O., & Alig, C. 2017, *MNRAS*, 464, 3536
- Rogers, H., & Pittard, J. M. 2013, *MNRAS*, 431, 1337
- Salpeter, E. E. 1955, *ApJ*, 121, 161
- Sana, H., de Mink, S. E., de Koter, A., et al. 2012, *Science*, 337, 444
- Schaller, G., Schaerer, D., Meynet, G., et al. 1992, *A&AS*, 96, 269
- Schaye, J., Crain, R. A., Bower, R. G., et al. 2015, *MNRAS*, 446, 521
- Schootemeijer, A., Langer, N., Grin, N. J., et al. 2019, *A&A*, 625, A132. doi:10.1051/0004-6361/201935046
- Shaviv, N. J. 2000, *ApJL*, 532, L137
- Smartt, S. J. 2015, *PASA*, 32, e016
- Smartt, S. J. 2009, *ARA&A*, 47, 63.
doi:10.1146/annurev-astro-082708-101737
- Smith, N. 2014, *ARA&A*, 52, 487
- Smith, N., & Owocki, S. P. 2006, *ApJL*, 645, L45
- Springel, V., Pakmor, R., Pillepich, A., et al. 2018, *MNRAS*, 475, 676
- Stinson, G., Seth, A., Katz, N., et al. 2006, *MNRAS*, 373, 1074
- Sukhbold, T., Ertl, T., Woosley, S. E., Brown, J. M., & Janka, H.-T. 2016, *ApJ*, 821, 38
- Sukhbold, T., & Woosley, S. E. 2014, *ApJ*, 783, 10
- Taam, R. E., & Sandquist, E. L. 2000, *ARA&A*, 38, 113
- Tailo, M., Milone, A. P., Lagioia, E. P., et al. 2021, *MNRAS*, 503, 694. doi:10.1093/mnras/stab568
- Tailo, M., Milone, A. P., Lagioia, E. P., et al. 2020, *MNRAS*, 498, 5745. doi:10.1093/mnras/staa2639
- Tailo, M., D'Antona, F., Vesperini, E., et al. 2015, *Nature*, 523, 318. doi:10.1038/nature14516
- Trampedach, R., Stein, R. F., Christensen-Dalsgaard, J., et al. 2014, *MNRAS*, 445, 4366. doi:10.1093/mnras/stu2084
- Trampedach, R., Stein, R. F., Christensen-Dalsgaard, J., et al. 2014, *MNRAS*, 442, 805. doi:10.1093/mnras/stu889
- Trampedach, R., Asplund, M., Collet, R., et al. 2013, *ApJ*, 769, 18. doi:10.1088/0004-637X/769/1/18
- Tramper, F. 2014, Ph.D. Thesis,
- Tramper, F., Sana, H., de Koter, A., & Kaper, L. 2011, *ApJL*, 741, L8
- van Loon, J. T. 2010, *Hot and Cool: Bridging Gaps in Massive Star Evolution*, 425, 279
- van Loon, J. T., Cioni, M.-R. L., Zijlstra, A. A., & Loup, C. 2005, *A&A*, 438, 273
- Vink, J. S. 2021, arXiv:2109.08164
- Vink, J. S. 2018, *A&A*, 619, A54
- Vink, J. S., Heger, A., Krumholz, M. R., et al. 2015, *Highlights of Astronomy*, 16, 51. doi:10.1017/S1743921314004657
- Vink, J. S., de Koter, A., & Lamers, H. J. G. L. M. 2001, *A&A*, 369, 574

- Vink, J. S., de Koter, A., & Lamers, H. J. G. L. M. 2000, *A&A*, 362, 295
- Vink, J. S., de Koter, A., & Lamers, H. J. G. L. M. 1999, *A&A*, 350, 181
- Walch, S., & Naab, T. 2015, *MNRAS*, 451, 2757

- Wang, L., Dutton, A. A., Stinson, G. S., et al. 2015, *MNRAS*, 454, 83
- Willson, L. A. 2000, *ARA&A*, 38, 573
- Yong, D., Norris, J. E., Bessell, M. S., et al. 2013, *ApJ*, 762, 26
- Yoon, S.-C., Woosley, S. E., & Langer, N. 2010, *ApJ*, 725, 940.
doi:10.1088/0004-637X/725/1/940

APPENDIX

A. WIND PRESCRIPTIONS

This appendix presents the details of the mass-loss rate and wind velocity functions that we adopt in our simulations.

A.1. Mass-loss rate

The settings of mass-loss rate in our simulations follow the wind schemes established in MESA. We apply the "Dutch" scheme for hot and WR winds and the dJ88 prescription for cool winds. The criteria to activate these winds are as follows:

- (1) If $T_{\text{eff}} > 12,000$ K, the "Dutch" scheme (*hot/WR wind*) is fully operating.
- (2) if $T_{\text{eff}} \leq 8,000$ K, the *cool wind* is fully operating, and the prescription of dJ88 is used.
- (3) Between 80,000 K and 12,000 K, a linear interpolation of the dJ88 (cool) and "Dutch" (mainly hot/ WR) winds is applied.

The "Dutch" scheme is not a single function, but a combination of V01's hot wind prescription, NL00's WR wind prescription, and the extension of dJ88's cool wind prescription. In detail, the wind configuration of the "Dutch" scheme is as follows:

- (1) If $T_{\text{eff}} \geq 11,000$ K and $X_H \geq 0.4$, the V01's hot wind prescription is adopted.
- (2) If $T_{\text{eff}} \geq 11,000$ K and $X_H < 0.4$, the NL00's WR wind prescription is adopted.
- (3) If $T_{\text{eff}} \leq 10,000$ K (low-T "Dutch" scheme), the dJ88 prescription, which is also used to express the cool wind, is adopted.
- (4) If $10,000 \leq T_{\text{eff}} \leq 11,000$ K, a linear interpolation of dJ88 and V01/NL00 prescriptions is adopted.

There are criteria to turn off the mass loss at the very end of the stellar lifetime. If the central temperature is higher than 2×10^9 K, mass loss will be fully turned off. If the central temperature is between 1×10^9 and 2×10^9 K, the mass-loss rate weakens linearly with the central temperature. These settings simply follow the default in MESA.

A.2. Wind velocity

As our MESA simulations do not include wind models, the wind terminal velocity (v_∞) is estimated using empirical functions of v_{esc} and other stellar parameters.

(1) *Hot wind.* If the V01's prescription of mass loss is turned on, we follow the wind velocity formulae adopted by Vink et al. (2001). These expressions originate from Leitherer et al. (1992) and Lamers et al. (1995).

a. If $T_{\text{eff}} > 27,500$ K, which is higher than the bi-stability jump, then

$$v_\infty/v_{\text{esc}} = 2.6(Z/0.019)^{0.13}. \quad (\text{A1})$$

b. If $T_{\text{eff}} < 22,500$ K, which is lower than the bi-stability jump, then

$$v_\infty/v_{\text{esc}} = 1.3(Z/0.019)^{0.13}. \quad (\text{A2})$$

c. If $22,500 < T_{\text{eff}} < 27,500$, the mass-loss rate is the linear combination of the high- T mass-loss rate (\dot{M}_h) and the low- T mass-loss rate (\dot{M}_l):

$$\dot{M} = \alpha\dot{M}_h + (1-\alpha)\dot{M}_l, \quad (\text{A3})$$

where $\alpha \equiv (T_{\text{eff}} - 22,500)/500$. The wind velocity we adopt is the weighted average of the high- T wind velocity ($v_{\infty,h}$) and the low- T wind velocity ($v_{\infty,l}$), and weighting coefficients are based on ratio of \dot{M} from high- and low- T components. The weighted average velocity \bar{v}_∞ can be expressed as

$$\bar{v}_\infty = \frac{\alpha\dot{M}_h v_{\infty,h} + (1-\alpha)\dot{M}_l v_{\infty,l}}{\alpha\dot{M}_h + (1-\alpha)\dot{M}_l}. \quad (\text{A4})$$

(2) *Cool wind.* We follow Leitherer et al. (1992) to set the cool wind velocity a constant 30 km s^{-1} . As long as the dJ88 prescription is used, even if it is called from the "Dutch" low- T scheme, we regard this part of mass loss as the cool wind.

(3) *WR wind*. We use the wind velocities given by [Nugis & Lamers \(2000\)](#) for WR stars.

a. WN stars:

$$\log(v_{\infty}/v_{\text{esc}}) = 0.61 - 0.13 \log L + 0.3 \log Y. \quad (\text{A5})$$

b. WC stars:

$$\log(v_{\infty}/v_{\text{esc}}) = -2.37 - 0.43 \log L - 0.07 \log Z. \quad (\text{A6})$$

In some transition temperatures, the mass-loss rate is composed of more than one wind component. In such cases, we use the ratios of mass-loss rates of these components as the weighting coefficients to calculate the average wind velocity. The expression is similar to Equation (A4), but with a linear combination of the hot/WR and cool wind velocities.